TECHNISCHE UNIVERSITÄT MÜNCHEN

WALTHER-MEISSNER-INSTITUT FÜR TIEF-TEMPERATURFORSCHUNG

BAYERISCHE AKADEMIE DER WISSENSCHAFTEN

Fabrication stability of Josephson junctions for superconducting qubits

Master's Thesis

Lujun Wang

Supervisor: Prof. Dr. Rudolf Gross

Munich, May 2015

Fakultät für Physik

Technische Universität München

Contents

List of Figures

Chapter 1

Introduction

Since introduced by Richard Feynman in 1982 [1, 2], quantum information processing (QIP) has become a highly active field of physics. In classical information processing, the elementary components for storing and manipulating information are bits, where each bit represents either a one or a zero. A quantum mechanical computer maintains a sequence of quantum bits (qubits) [3–5]. A single qubit can not only represent either of those two states, but also an arbitrary combination of the two, a superposition state. Together with entanglement, another peculiar property of quantum mechanics, the superposition states allow for a much more powerful information platform than is possible with classical components.

Superconducting quantum circuits are one of the most promising platforms for realizing QIP. They have some important advantages over natural atoms, e.g. the strong coupling to the environment and the possibility to be lithographically designed to have specific characteristics, such as a large dipole moment or particular transition frequencies [6]. There are several different types of superconductiong qubits, such as charge qubit, flux qubit, phase qubit, etc [7]. At the WMI, flux qubits [8, 9] are employed for experiments. This type of qubit consists of two identical Josephson junctions and one with a smaller area. Josephson junctions, which are nonlinear elements based on the Josephson effect [10], are the key elements of these superconducting quantum circuits. A Josephson junction is a sandwich structure of two superconductors with a thin layer of insulating material in between. Usually, type-I superconductors are used as junction electrodes due to their high quality and easy fabrication. Among the metal Josephson junctions, $Al/AlO_x/Al$ junctions are the most widely used because of the relatively long coherence times of the qubits they form [11]. Previous studies of the Josephson junction fabrication have been done at the WMI [12–15]. However, fabrication is still a challenge because the properties of the qubits are ultra-sensitive to the fabrication parameters and to realize a universal quantum computer in the future, a large number of well-controlled Josephson junctions and the scalability of the number of qubits are required [16]. Moreover, the fabrication process is very sensitive to the conditions of the equipments and the local environment.

In this thesis, several efforts are made to improve the fabrication stability of Josephson junctions. Recently, a new spin coater and a new electron beam lithography (EBL) system

have been installed at the WMI. We here make some tests of these two devices and evaluate the improvements they bring to our fabrication routine. We also try to find a proper hard mask to protect the shadow evaporation mask during the cleaning of the substrate or metal interface before Al evaporation. Furthermore, a new rule for estimating the critical current density from the oxidation parameters will be set up here.

The thesis is organized as follows: a short introduction to the theoretical background of superconductivity and the Josephson junction is given followed by a brief discussion of the dc SQUID and superconducting qubits (Ch. 2). Chapter 3 describes the basic principle of the experimental techniques and setups used for fabricating and investigating the Josephson junctions. Subsequently, the fabrication process with improvements for each step and the main experimental results obtained during this work are presented and analyzed in Ch. 4. Finally, a summary of our studies is given followed by an outlook onto future plans regarding the fabrication stability of Josephson junctions (Ch. 5).

Chapter 2

Theory

In this chapter, the basic theory aspects underlying this work are presented. We begin with a brief introduction to superconductivity. Then, Josephson junctions, the essential elements in our fabricated samples, are discussed. Next, the application of Josephson junctions in dc SQUIDs is investigated. At last, the physics of superconducting flux qubit is explained.

2.1 Superconductivity

Superconductivity is a thermodynamic phase of certain materials. When they are cooled below a characteristic critical temperature T_c, their electrical resistance becomes zero and external magnetic fields are expelled. The zero resistance phenomenon was first discovered by Dutch physicist Heike Kamerlingh Onnes in 1911 [17] while the effect of expulsion of magnetic fields was discovered by Walther Meissner and Robert Ochsenfeld in 1933 [18].

In a superconductor, due to the mediation by phonons [19], electrons close to the Fermi energy level form phase correlated Cooper pairs [20] which are subjected to the Bose-Einstein statistics. According to the BCS-theory [21], at zero temperature all the Cooper pairs occupy the same energy state which is separated from all higher states by the superconducting gap. This means, the Cooper pairs form a condensate which can be described by a macroscopic wave function [22]:

$$\Psi(\mathbf{r},t) = \Psi_0(\mathbf{r},t) \cdot \exp(i\phi(\mathbf{r},t)) = \sqrt{n_s(\mathbf{r},t)} \cdot e^{i\phi(\mathbf{r},t)}, \tag{2.1}$$

with $n_s(\mathbf{r},t)$ being the local macroscopic density of Cooper pairs and $\phi(\mathbf{r},t)$ the time dependent macroscopic phase.

2.2 The Josephson junction

Josephson junction (JJ) is a device consisting of two superconductors coupled by a weak link. The weak link can be a thin insulating barrier, a short section of non-superconducting metal or a physical constriction that weakens the superconductivity at the point of contact.

In this work, junctions with a thin insulating barrier are adopted, known as superconductor-insulator-superconductor (SIS) junctions. The schematic drawing of a Josephson junction and the SEM image of a typical junction fabricated in this work are shown in Fig. 2.1.

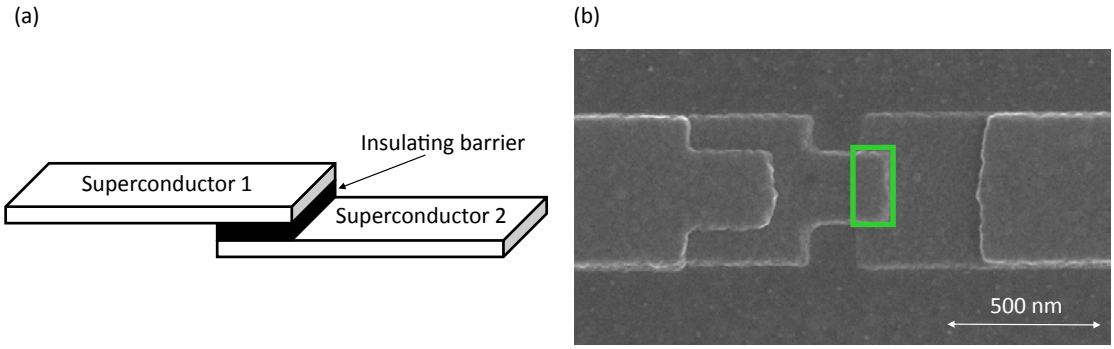

Figure 2.1: **(a)** Schematic drawing of a Josephson junction. **(b)** SEM micrograph of a Josephson junction fabricated in this work which is realized as two superconducting Al layers separated by a nm thick Al oxide layer. The actual junction area is marked with a green box. The duplicated structures are due to the shadow evaporation under different angles.

The phenomenon of the supercurrent tunneling from one superconductor through the thin barrier to the other superconductor, named as Josephson effect, has been predicted by British physicist Brian D. Josephson theoretically in 1962 [23]. The tunneling can happen because the insulating barrier is thin enough so that the macroscopic wavefunctions Ψ_1 and Ψ_2 of the two superconductors can overlap [24].

2.2.1 Josephson equations

For the current and voltage across the barrier, Brian D. Josephson has given the mathematical relationships, which are known as Josephson equations:

$$I_\mathrm{s} = I_\mathrm{c} \cdot \sin(\varphi) \tag{2.2}$$

$$\frac{\partial \varphi}{\partial t} = \frac{2\pi}{\Phi_0} V \tag{2.3}$$

where I_c is the critical current, $\varphi = \phi_2 - \phi_1$ is the phase difference between the two superconductors, Φ_0 is the magnetic flux quantum and V is the voltage across the junction.

The first Josephson equation describes the current-phase relation of the system and the second Josephson equation describes the voltage drop over the barrier when the phase difference evolves in time. If we take the time derivative of the first Josephson equation and plug in the second one, the junction can also be described as a highly non-linear inductance which makes it a fundamental element for superconducting qubits.

$$\frac{dI}{dt} = I_\mathrm{c}\cos(\varphi)\frac{2\pi}{\Phi_0}V = \frac{1}{L}V \tag{2.4}$$

$$L = \frac{\Phi_0}{2\pi I_\mathrm{c}\cos(\varphi)} \equiv L_c\frac{1}{\cos(\varphi)} \tag{2.5}$$

The thickness d of the insulating tunneling barrier determines the critical current density J_c [22]. If we solve the Schrödinger equation for the macroscopic wave function of each side by the wave matching method, we can get the current density:

$$J_\mathrm{s} = \frac{e\hbar\kappa}{m_\mathrm{e}}\frac{\sqrt{n_1 n_2}}{\sinh(2\kappa d)}\sin(\varphi) \equiv J_\mathrm{c}\sin(\varphi) \tag{2.6}$$

where κ is a characteristic decay constant which is a property of the barrier:

$$\kappa = \sqrt{\frac{4m_\mathrm{e}(V_0 - E_0)}{\hbar^2}}\,. \tag{2.7}$$

Here, E_0 is the kinetic energy of the superelectrons and V_0 is the barrier height. As discussed later in Sec. 4.4, the barrier thickness d is in the order of few nm and the barrier height V_0 is usually a few meV for the junctions investigated in this work.

2.2.2 Characteristic energies

There are two characteristic energy scales to be considered for a Josephson junction. First, we find the coupling energy E_J. It is the binding energy of the two superconductors due to the overlapping of their macroscopic wave functions. By using the two Josephson equations, the potential energy of a Josephson junction can be defined as:

$$\widetilde{U}(\varphi) = \int_0^{t_0} I_\mathrm{s}V\,dt = \frac{\Phi_0 I_\mathrm{c}}{2\pi}(1-\cos(\varphi)) \equiv E_\mathrm{J}(1-\cos(\varphi))\,. \tag{2.8}$$

with E_J as the Josephson coupling energy.

The second energy scale is the capacitive energy E_C. Since Josephson junctions consist of two metal faces separated by an insulator, they also act as a capacitor. The corresponding energy scale is called charging energy and defined as:

$$E_\mathrm{C} \equiv \frac{e^2}{2C}. \tag{2.9}$$

Here, C is the capacitance of the junction defined by its geometry.

2.2.3 Current-voltage characteristics

Current-voltage characteristics are applicable to any electrical system. However, in Josephson junctions current and voltage typically oscillate due to the Josephson equations.

Hence, the current-voltage characteristics feature time-averages quantities. In a typical I-V curve of a Josephson junction, there is no voltage drop over the junction when the bias current is increased from zero up to a critical value I_c. This state is the zero-voltage state of the junction. If the current is increased beyond I_c, the junction switches to the voltage state with a material specific gap voltage of

$$V_g = \frac{2\Delta}{e}, \tag{2.10}$$

which is approximately 365 µV for aluminium [25]. In this case, the junction becomes normal conducting with a resistance R_n. This effect occurs because the Cooper pairs are broken up and single electrons account for a normal conducting current. If the current is then decreased from the voltage state, the voltage jumps back to zero at the retrapping current $I_{re} \leq I_c$ [26]. A theory by Ambegaokar and Baratoff gives the relation of the critical current I_c, the normal resistance R_n and the energy gap Δ [27]:

$$I_c R_n = \frac{\pi\Delta}{2e} = \frac{\pi}{4} V_g \,. \tag{2.11}$$

The product of $I_c R_n$ is also called characteristic voltage V_c. It serves for proving the quality of a Josephson junction.

2.2.4 RCSJ model

The physics behind Josephson junctions can be described by the resistively and capacitively shunted junction model (RCSJ-model), introduced by Stewart and McCumber in 1968 [28]. In this model, the Josephson junction is represented by an equivalent electrical circuit consisting of a nonlinear inductance L_J, a normal resistance R_n and a junction capacity C where noise sources are ignored intentionally in order to maintain simplicity. These elements are connected in parallel and biased by a current I (cf. Fig. 2.2).

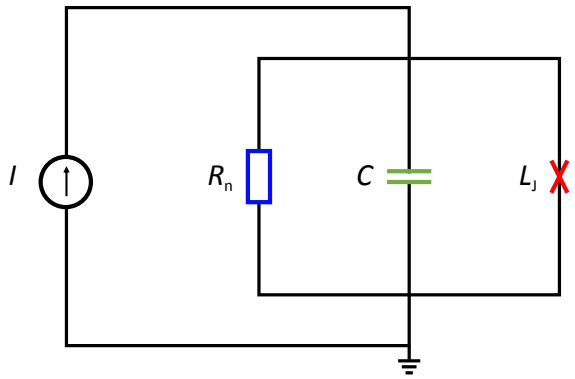

Figure 2.2: Scheme of the RCSJ-model for a Josephson junction: The circuit consists of a nonlinear inductance L_J, a normal resistance R_n and a junction capacity C.

According to Kirchhoff's law of current conservation, the total current I supplied by the

bias source splits into three parts. They are the supercurrent $I_\mathrm{s} = I_\mathrm{c}\sin(\varphi)$ flowing across the nonlinear inductance, the current $I_\mathrm{n} = V/R_\mathrm{n}$ flowing across the normal resistance and the displacement current $I_\mathrm{d} = C\,dV/dt$ flowing across the capacitor. If we substitute V with the second Josephson equation (2.3), the junction dynamics can be described with the equation

$$I = I_\mathrm{c}\sin(\varphi) + \frac{V}{R_\mathrm{n}} + C\frac{dV}{dt} = I_\mathrm{c}\sin(\varphi) + \frac{1}{R_\mathrm{n}}\frac{\Phi_0}{2\pi}\frac{d\varphi}{dt} + C\frac{\Phi_0}{2\pi}\frac{d^2\varphi}{dt^2}, \tag{2.12}$$

which is a nonlinear differential equation. By rewriting the equation and plugging in the Josephson coupling energy $E_\mathrm{J} = \Phi_0 I_\mathrm{c}/2\pi = \hbar I_\mathrm{c}/2e$, we get

$$\left(\frac{\hbar}{2e}\right)^2 C\,\frac{d^2\varphi}{dt^2} + \left(\frac{\hbar}{2e}\right)^2 \frac{1}{R_\mathrm{n}}\frac{d\varphi}{dt} + \frac{d}{d\varphi}[E_\mathrm{J}\cdot(1-\cos(\varphi) - \frac{I}{I_\mathrm{c}}\varphi)] = 0\,. \tag{2.13}$$

This equation of motion is analogous to that of a damped mechanical oscillator,

$$M\frac{d^2x}{dt^2} + \eta\frac{dx}{dt} + \nabla U = 0\,. \tag{2.14}$$

The effective mass M, damping η and potential U are

$$M = \left(\frac{\hbar}{2e}\right)^2 C \quad , \quad \eta = \left(\frac{\hbar}{2e}\right)^2 \frac{1}{R_\mathrm{n}} \quad \text{and} \quad U = E_\mathrm{J}(1-\cos(\varphi) - \frac{I}{I_\mathrm{c}}\varphi)\,. \tag{2.15}$$

The potential described in Eq. (2.15) is a so called washboard potential and is plotted in Fig. 2.3. In the washboard potential, the phase φ behaves as a virtual particle. When $I < I_\mathrm{c}$, the phase does not evolve in time because the phase particle is trapped in a local potential minimum. Therefore, there is no voltage drop across the junction according to the second Josephson equation. When $I > I_\mathrm{c}$, the washboard becomes tilted to an extent that local potential minima do not exist anymore. The phase particle moves continuously down the tilted washboard making the phase evolve in time and thus gives rise to a voltage drop. If we want the junction to return to the superconducting state, which means the phase particle getting trapped into a potential minimum again, the applied dc current needs to be reduced to $I_\mathrm{re} \leq I_\mathrm{c}$ due to the gained kinetic energy of the phase particle.

To describe how a junction can return from voltage state to superconducting state, the Stewart-McCumber parameter β_C is introduced:

$$\beta_\mathrm{C} = \frac{2\pi I_\mathrm{c} R_\mathrm{n}^2 C}{\Phi_0}\,. \tag{2.16}$$

If $\beta_\mathrm{C} \gg 1$ (underdamping), this situation can be described as a heavy particle moving in a shallow potential. Due to its large kinetic energy, the particle will not stop until the potential is brought back to the horizontal state ($I_\mathrm{re} = 0$). For $\beta_\mathrm{C} \ll 1$ (overdamping), the particle is light while the damping is large. Therefore, the particle can be stopped

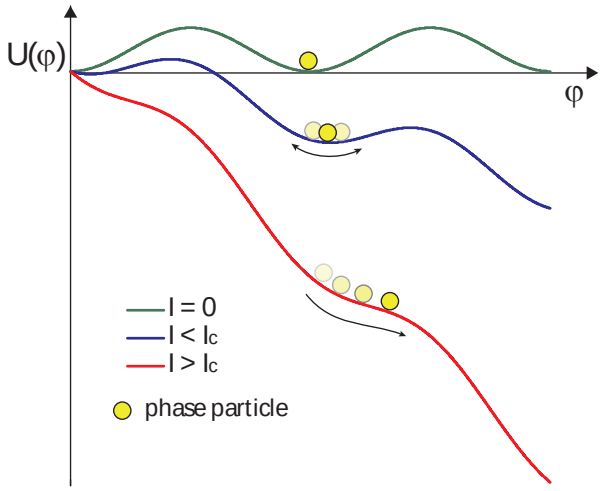

Figure 2.3: Plot of washboard potential: For $I = 0$ (green curve), the phase particle is trapped in a potential minimum. For $I < I_c$ (blue curve), the potential is slightly tilted and the phase particle can tunnel through the lowered potential barrier. For $I > I_c$ (red curve), there is no potential minimum anymore and the phase particle moves continuously down the potential. Correspondingly, the junction switches to the voltage state.

immediately when the potential is tilted back below I_c and shallow minima form ($I_{re} = I_c$). For intermediate damping, one finds $0 \leq I_{re} \leq I_c$.

2.3 The dc SQUID

A superconducting quantum interference device (SQUID) can be utilized to measure small magnetic fields. In this thesis, however, we use the dc SQUID, which is made of a superconducting loop interrupted by two Josephson junctions connected in parallel (cf. Fig. 2.4), to characterize the properties of the fabricated Josephson junctions.

The physics behind a dc SQUID can be simplified as the phase interference of the wave functions in its two branches. To theoretically describe the dc SQUID, both junctions are assumed to be identical and small compared to the size of the loop. Therefore, both junctions have the same critical current I_c and effects of magnetic flux penetrating the junctions can be neglected.

According to Kirchhoff's law, the total supercurrent I_s can be expressed with this equation:

$$I_s = I_c \sin(\varphi_1) + I_c \sin(\varphi_2) = 2I_c \cos\left(\frac{\varphi_1 - \varphi_2}{2}\right) \sin\left(\frac{\varphi_1 + \varphi_2}{2}\right) . \tag{2.17}$$

To calculate the phase difference, we integrate the phase gradient over the dc SQUID loop $\varphi = \int \nabla\phi(\mathbf{r},t) \cdot d\mathbf{l}$. If we choose the integration path deep inside the superconductor, where $J_s = 0$, we obtain a phase difference which depends only on the flux Φ going through

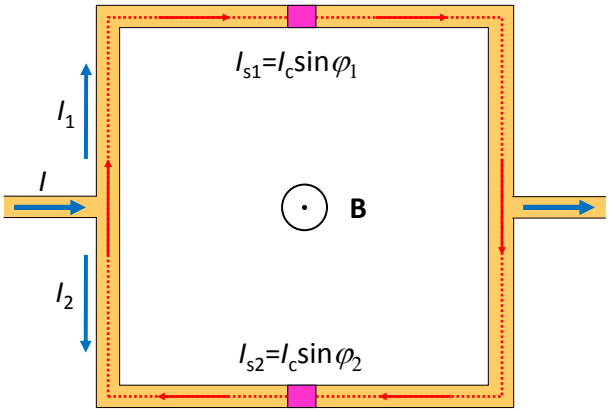

Figure 2.4: Sketch of a dc SQUID: The applied current splits into two parts I_1 and I_2. In the presence of magnetic field, the phase difference for both junctions (pink) is φ_1 and φ_2, respectively. The dashed line indicates the integration path for calculating the total phase difference

the dc SQUID loop:

$$\varphi_1 - \varphi_2 = \frac{2\pi\Phi}{\Phi_0}. \tag{2.18}$$

We rewrite Eq. (2.17) by plugging in the phase difference:

$$I_\mathrm{s} = 2I_\mathrm{c}\cos\left(\pi\frac{\Phi}{\Phi_0}\right)\sin\left(\varphi_2 + \pi\frac{\Phi}{\Phi_0}\right). \tag{2.19}$$

Therefore, the maximum supercurrent $I_\mathrm{s}^\mathrm{max}$ is dependent on the flux penetrating the loop:

$$I_\mathrm{s}^\mathrm{max}(\Phi) \equiv 2I_\mathrm{c}\left|\cos\left(\pi\frac{\Phi}{\Phi_0}\right)\right|. \tag{2.20}$$

The pattern of $I_\mathrm{s}^\mathrm{max}$ is plotted in Fig. 2.5(a) which is similar to the interference pattern of a double-slit experiment shown in Fig. 2.5(b). The phase difference in a dc SQUID, which is tuned by external magnetic flux, is analogous to the the phase difference of the two beams in a double-slit experiment, which is set by a variation in the beam paths.

Self inductance of the dc SQUID

In the discussion above, the self inductance of the dc SQUID is neglected. The maximum supercurrent $I_\mathrm{s}^\mathrm{max}$ can be modulated from $2I_\mathrm{c}$ down to zero, which is denoted by the black curve ($\beta_\mathrm{L} = 0$) in Fig. 2.5(a). β_L is the screening parameter to describe the self inductance:

$$\beta_\mathrm{L} \equiv \frac{2LI_\mathrm{c}}{\Phi_0} \tag{2.21}$$

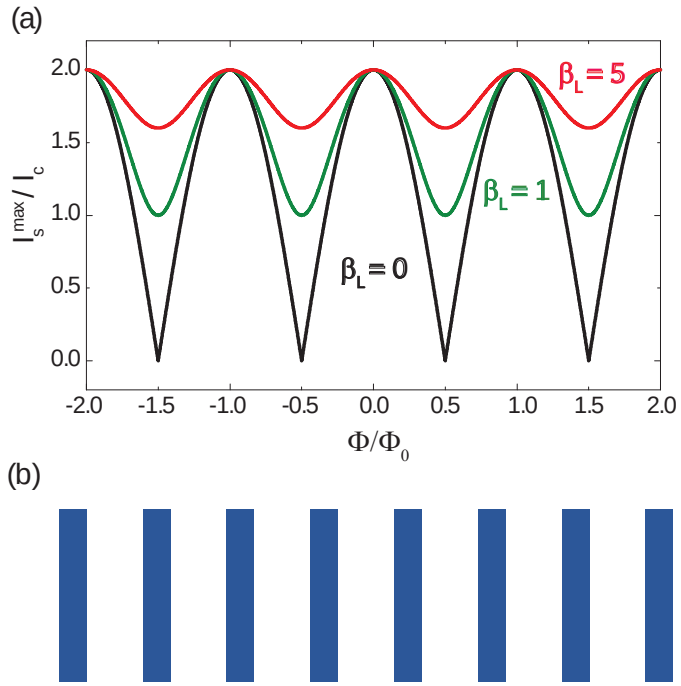

Figure 2.5: **(a)** Plot of the interference pattern of a dc SQUID: The maximum supercurrent I_s^{max} is dependent on the flux Φ penetrating the dc SQUID loop. Three cases with different screening parameter β_L are shown. **(b)** Schematic pattern of a typical double-slit interference experiment.

which is the ratio between the maximum magnetic flux generated by the loop LI_c and half a flux quantum.

If we take the self inductance into consideration, the flux generated by the circulating current I_{circ} in the loop with inductance L should be included in the total flux Φ together with the external flux Φ_{ext}:

$$\Phi = \Phi_{ext} + LI_{circ} \,. \tag{2.22}$$

Hence, the maximal modulation amplitude of $2I_c$ cannot be reached even at zero external flux. When the self inductance is sufficiently large, even small circulating currents $I_{circ} \ll I_s^{max}$ can lead to $\beta_L \gg 1$. The maximum supercurrent range is approximately inversely proportional to β_L [29]:

$$\frac{\Delta I_s^{max}(\Phi)}{2I_c} \approx \frac{1}{\beta_L} \tag{2.23}$$

where $\Delta I_s^{max}(\Phi)$ is the difference between the maximal and the minimal values for the maximum supercurrent with regard to Φ. Nevertheless, a full modulation of I_s^{max} in dependence of Φ can be measured for $\beta_L \leq 2/\pi$.

Chapter 3

Experimental techniques

The fabrication of Josephson junctions consists of several different steps. In this chapter, we give a short introduction to the devices used for fabricating Josephson junctions and to the method for evaluating the junction quality. First, the spin coating process and the features of our new spin coater are presented. Then, we describe the basic principles of EBL and the advantages of our new EBL system. Next, the shadow evaporation technique and the home-made evaporation system are shown. Finally, we discuss the testing of the fabricated Josephson junctions by cryogenic characterization of dc SQUIDs.

3.1 Spin coating

To fabricate Josephson junctions using shadow evaporation, two different sub-micrometer thin layers of resist are required. The top layer defines the shadow mask which is suspended in certain areas by an undercut in the bottom layer resist. A common technique to produce such thin resist films on planar substrates is spin coating. The homogeneity of the thin films is essential for the reproducibility of the junction area. In the following section, relevant basic theory of spin coating is presented. In addition, we also discuss features of the new spin coater relevant for a stable fabrication.

3.1.1 Spin coating process

A typical spin coating process includes several key stages. First, a small puddle of liquid resist is dispensed onto a substrate, then the substrate is spun up to a certain speed (typically some 1000 rpm). As a consequence of centrifugal acceleration, the resist will spread towards, and eventually off, the edge of the substrate leaving a thin film of resist on the surface. This process is dependent on the viscous forces inside the liquid resist. After this step, we keep spinning at a constant speed for some time to dry the film while the solvent evaporation dominates the thinning behavior in this stage [30]. Figure. 3.1 shows the spin coating process schematically.

The parameters, such as acceleration, final spin speed and spin time, chosen for the spin process and the nature of the resist such as evaporation rate, viscosity, solution

concentration will determine the final film thickness and other properties. Reproducibility of high quality resist films in terms of homogeneity and surface evenness is very important for a stable fabrication of Josephson junctions. Drastic variations in the coated film can be caused by subtle variations in the parameters that define the spin process. Some effects of these variations are discussed in the following section.

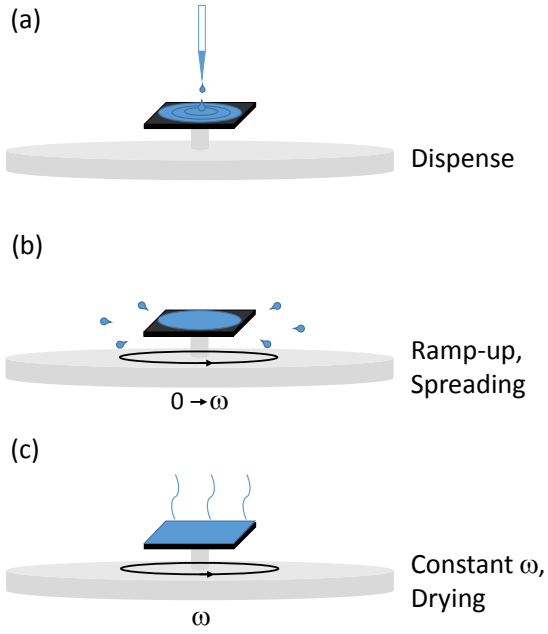

Figure 3.1: Schematic drawing of spin coating process: **(a)** The resist fluid is deposited onto the substrate surface. **(b)** A high speed spin step to thin the fluid. **(c)** A drying step to eliminate excess solvents from the resulting film.

3.1.2 Key factors in spin coating

Spin speed

Spin speed is one of the most important factors in spin coating. Not only is the degree of radial force applied to the liquid resist determined by the spin speed, but also the velocity and characteristic turbulence of the air immediately above the resist are affected. In particular, the high speed spin step generally determines the final film thickness. Relatively minor variations of ±50 rpm at this stage can cause a resulting thickness change of 10% [31]. A general film thickness trend chart over spin speed is depicted in Fig. 3.2(a).

Spin time

The final film thickness is basically a balance between the centrifugal force and the viscous force. As the resist dries, the viscosity increases until the radial force of the spin process can no longer appreciably move the resist over the surface. To achieve this point, the

high speed spin step should run for a sufficiently long time. After this, the film thickness will not decrease significantly with increased spin time. Figure 3.2(b) shows the thickness trend chart over time.

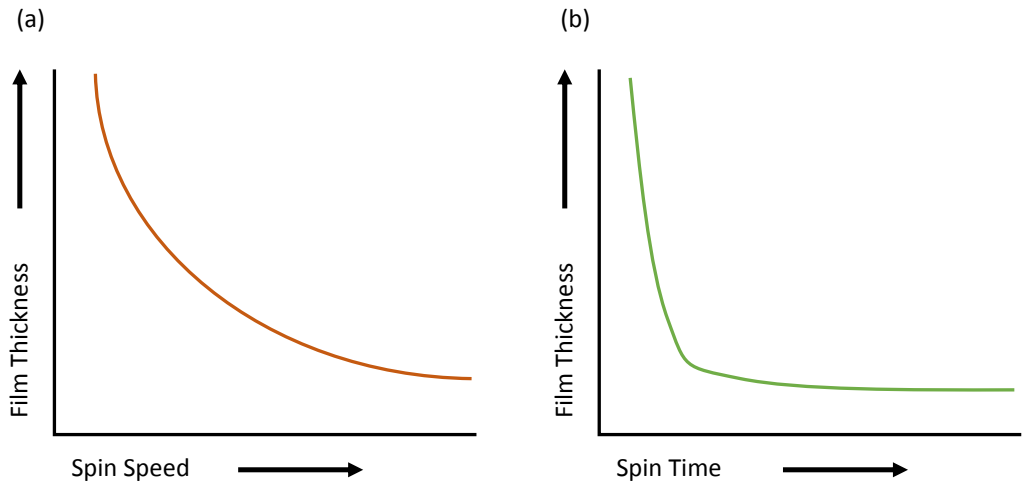

Figure 3.2: Spin coating process trend charts: For most resist materials the final film thickness is inversely proportional to the spin speed and spin time.

3.1.3 Features of new spin coater

The new spin coater, Laurell WS-650, employs a "closed bowl" design and has a constant inside nitrogen flow, which keeps the ambient conditions constant during the spin coating process (cf. Fig. 3.3b). This design brings two different advantages. First, the constant

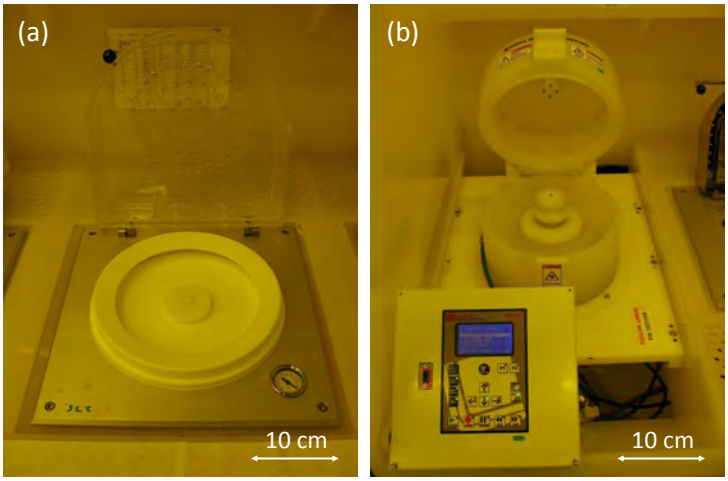

Figure 3.3: Photograph of spin coater: **(a)** Old spin coater with a lid open to the environment. **(b)** New spin coater with a closed bowl.

nitrogen atmosphere makes the drying of the resist take place in a much more controlled manner. This offers the advantage of reproducibility from run to run.

Another benefit of this design is that it can protect the air flow around the spinning substrate. By closing the bowl with a smooth lid surface, variations and turbulence caused by the air-conditioning in the clean room and the presence of operators and other equipment have only a reduced influence on the spin process. Thus, the film thickness uniformity will be less affected by these uncertainties.

3.2 Electron beam lithography

EBL is a common technique in nanofabrication. It has the ability to create arbitrary two-dimensional patterns with precisions down to the nanometer scale because of the electrons' short wavelength. This property makes it suitable for fabricating Josephson junctions. To ensure the fabrication stability of Josephson junctions, precisely defined resist masks are required. This section gives a short introduction to the basic principles of EBL and also some features of our new EBL system.

3.2.1 Basic principles of EBL

The technique behind EBL is accurately controlling a highly focused electron beam to expose a resist film in order to dramatically modify the solubility of the resist material during a subsequent development step (cf. Fig. 3.4).

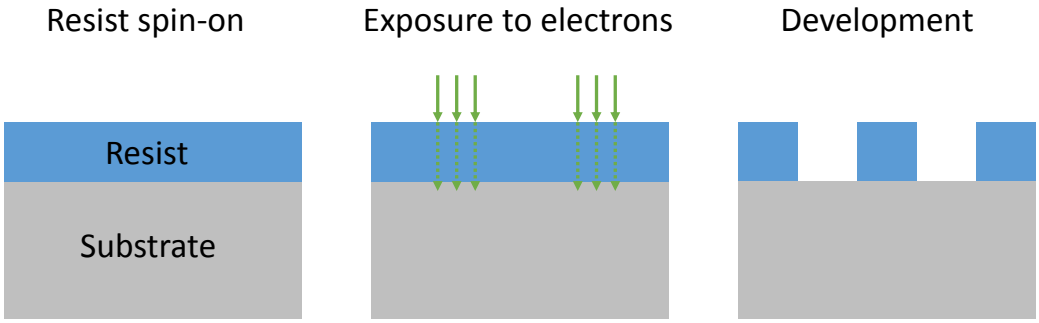

Figure 3.4: Outline of EBL process to generate a nanoscale pattern on a positive resist film.

Originally, EBL has been developed from the scanning electron microscopes to which a pattern generator (consisting of a beam blanker and a deflection system) and a precisely moving stage are added to control which areas on the resist to be exposed. The schematic diagram of the system is depicted in Fig. 3.5. The pivotal determinant of the electron beam resolution will be the quality of the electron optics in terms of the ability to create a fine focused spot. Process conditions such as the electron beam energy and dose, the chosen developer and development time also play vital roles.

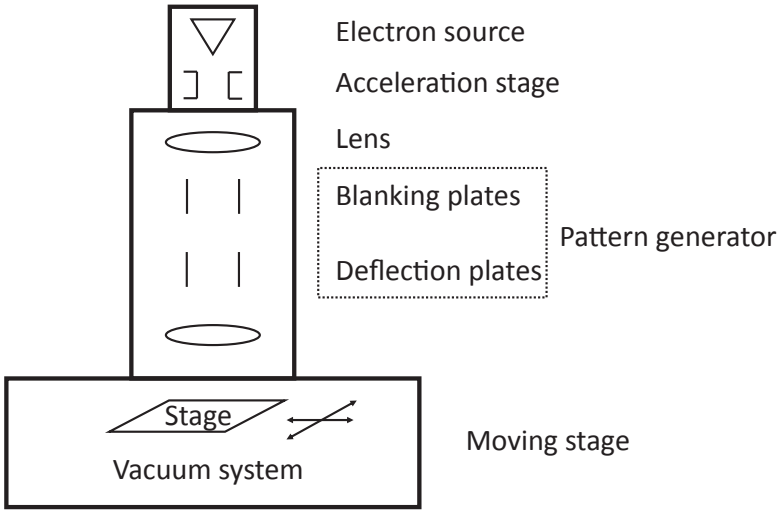

Figure 3.5: Schematic diagram of EBL system

3.2.2 Features of new EBL system

In 2014, a new EBL system, nB5 from NanoBeam Ltd., has been installed at the WMI (cf. Fig. 3.6). The system consists of three main parts. On the top, there is the thermal field

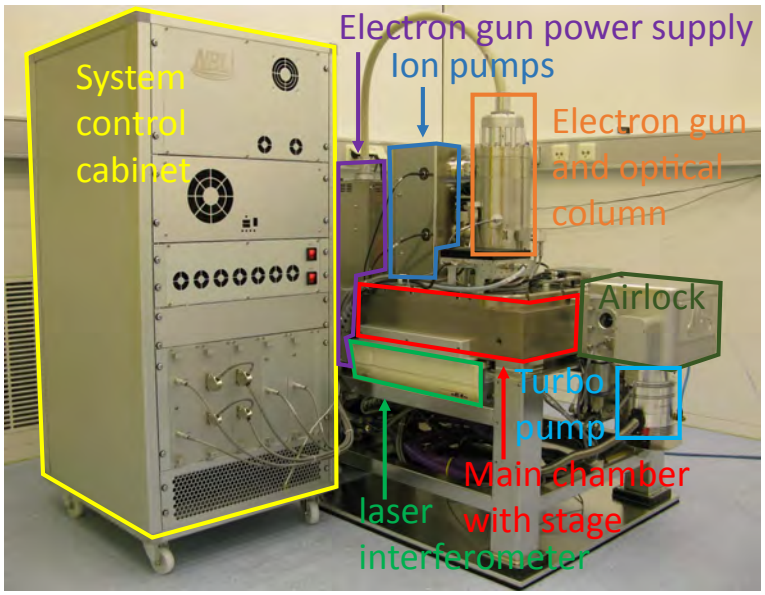

Figure 3.6: Photograph of the EBL system at the WMI: nB5 from NanoBeam Ltd.

emitter electron source with low coulomb-effect electron optics and sophisticated column designs which enables it to provide an electron beam with guaranteed beam size of <5 nm while the beam current and voltage can range from 0.1 nA to 100 nA and 20 kV to 100 kV, respectively [32]. One of the key features is the dual-deflection system which is controlled

by two independent deflection sub-systems. The total deflection coverage is split up into mainfield and subfield in order to achieve ultra-high deflection speed for beam writing in the end. Another essential technique is the conjugate blanking which can cancel the blanking voltage ringing and eliminate the blanking drift. The blanking plates are placed at the conjugate point of the lens. This means the beam at the target stays at its position during blanking which would otherwise leave streaks in the resist. The next part is an XY stage tracked by a high speed laser interferometer with positioning resolution of <1 nm. This tracking system also gives feedback for tracking the stage vibration dynamically and correcting the stage movements. The last part is the multi-chuck airlock and auto-loading robot which is essential for automatic operation and continuous writing [33]. Furthermore, each chuck contains multiple slots for different wafers (cf. Fig. 3.7).

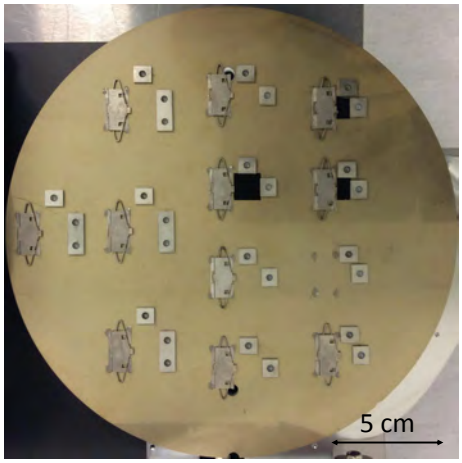

Figure 3.7: Photograph of a chuck with multiple slots: The four slots on the right are for 6 mm×10 mm substrates. The row in the middle are four 12 mm×12 mm slots. The last four slots on the left are 12 mm×24 mm in dimension.

To some extent, the beam quality is the key factor which will affect the result of writing. According to the company, this EBL system has a beam size of approximately 5 nm with zero beam scattering during writing [33]. As a result, the profile of the beam is extremely focused which will generate straight edges on exposed resist (cf. Fig. 3.8). Therefore, it is possible to get reproducible results and make the post wafer processing such as resist development far less susceptible to time.

At last, the required cleanroom conditions for this system, such as room temperature variation, magnetic stray field, and floor vibration, are not as demanding as for other EBL systems [33]. And for the user's side, it is very easy to operate because of the nicely designed software and user interface. We can focus on the sample very easily either automatically by using on-chip focus marks or manually with help of gold particles. Former manual corrections such as adjusting astigmatism, setting the beam current, calibrating and aligning the beam are now done by a software command. All these features of the electron optics and automation system enhance its throughput and reliability in the end.

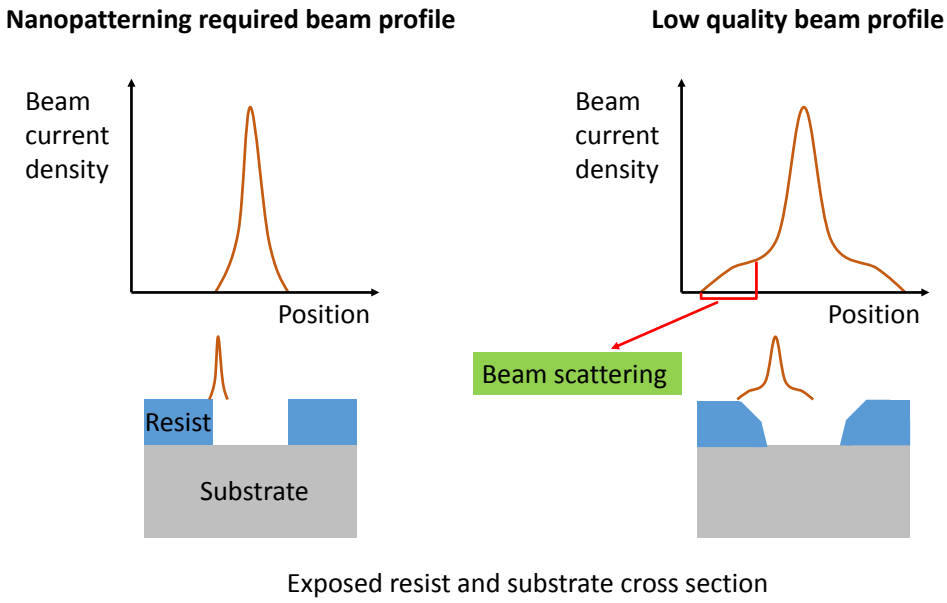

Figure 3.8: Demonstration of different beam profiles and generated edges on exposed resist.

3.3 Evaporation and Oxidation

Evaporation is commonly used in microfabrication to deposit thin films of metal. In an ultra-high vacuum the source material is heated and melted by a high current electron beam. Then vapor particles can travel directly to the target substrate, where they condense back to solid state as an uniform thin layer.

In the following section, we cover the process of the special technique, so-called shadow evaporation, for fabricating Josephson junctions and the properties of the evaporation system used at the WMI.

3.3.1 Shadow evaporation and in-situ oxidation

A well-known approach to fabricate Al/AlO_x/Al Josephson junctions is the shadow evaporation technique using a micro-fabricated bridge [34]. This method can produce Josephson junctions with high quality leading to longer qubit coherence times.

First of all, we need a substrate with double layer resist which is patterned by EBL beforehand. The top resist plays the role of the mask with a suspended bridge which generates a shadow on the substrate surface while the bottom layer serves as the support with undercut. Then, the substrate is loaded into the evaporation chamber for evaporation and oxidation. This process is schematically illustrated in Fig. 3.9.

When the first layer of aluminum is evaporated onto the substrate under an angle, because of the existence of the bridge the deposited layer is interrupted. This first layer of aluminum film is then subjected to an oxidation process at a constant pressure by

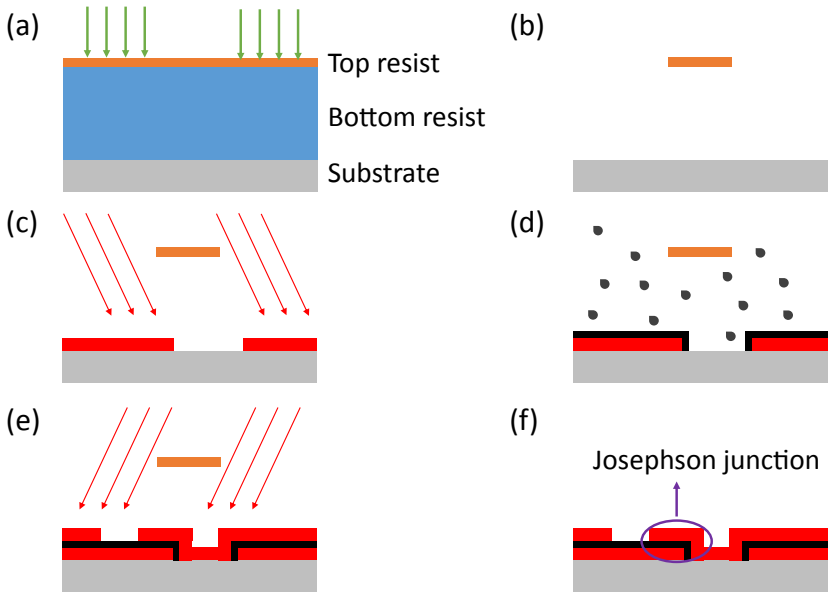

Figure 3.9: Schematics of Al/AlO_x/Al junction shadow evaporation fabrication process: **(a)** EBL writing, **(b)** development, **(c)** first Al layer evaporation, **(d)** oxidation, **(e)** second Al layer evaporation, **(f)** lift-off.

letting oxygen into the UHV chamber and pumping it at a constant pumping power. This method creates a dynamical pressure equilibrium. After a certain time, a very thin layer of AlO_x will be formed on the surface. Then, a second layer of aluminum film is deposited right after the oxidation process from the angle in order to create an overlap. This overlap under the bridge separated by the thin AlO_x layer results in the Al/AlO_x/Al Josephson junction. At the end, all the resist and unwanted aluminum film are removed by lift-off.

3.3.2 Evaporation system at the WMI

For the special purpose of shadow evaporation and controlled oxidation process, a dedicated electron beam evaporation system has been developed at the WMI (cf. Fig. 3.10).

To obtain high junction quality, the evaporation and oxidation parameters must be controlled precisely. Several measures need to be taken to meet this requirement. First, the aluminum used in our system has a purity of 99.999%. It consists of small aluminum slugs pre-melted in a crucible. The pre-melting is done by sweeping the electron beam manually across the whole crucible to create an homogeneous melt. As a result, the actual evaporation rate is very stable and can be controlled accurately by changing the current of the electron beam.

The evaporation chamber is pumped by a turbo pump to reach an ultra-high vacuum of pressure $< 10^{-8}$ mbar. Inside the chamber the substrate can be rotated to different angles by a motorized manipulator enabling shadow evaporation. Moreover, a relatively long distance of 65 cm is given between the evaporation source and the substrate to avoid

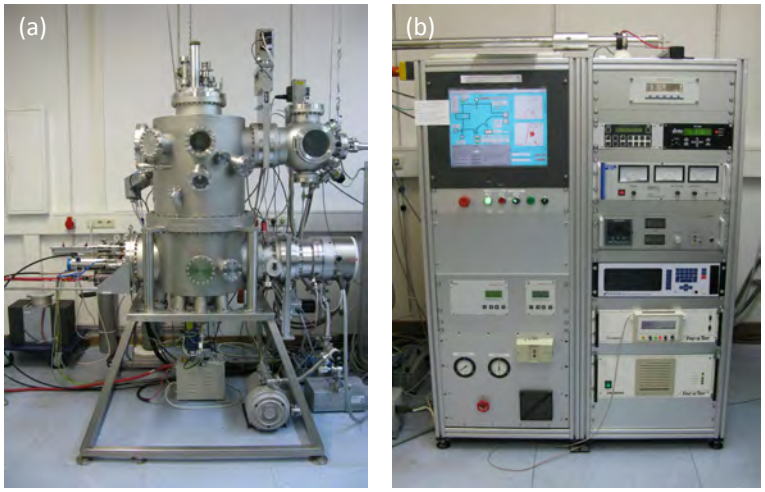

Figure 3.10: Photograph of evaporation system: **(a)** Evaporation chamber. **(b)** Required electronic devices for controlling the process.

heating effects. In order to measure and control the thickness of the grown aluminum films, a piezoelectric quartz crystal sensor is installed inside the chamber. For oxidation, a constant oxygen flow is let into the chamber with the help of a mass flow controller. To achieve a certain stable oxygen pressure, we can adjust the valve in front of the turbo pump. Different pressure sensors are also installed inside the chamber for monitoring the pressure during the process.

The whole system including all the sensors and devices is controlled by a computer with a LabView program. That means the evaporation and oxidation process can be conveniently and automatically controlled. This program also contains several algorithms which maintain the fabrication safety and reproducibility. A sufficiently low pressure should be reached before the evaporation starts and the evaporation rate fluctuation should be in a certain range before the shutter opens and lets the vapor particles travel to the target substrate. Furthermore, the real-time values of the important process parameters, such as evaporation rate, oxygen flow and pressure are recorded in the log files for post-process analysis.

3.4 Cryogenic characterization of dc SQUIDs

The Josephson junctions are incorporated into a dc SQUID in order to test their properties. In qubit applications, the most important parameter of a Josephson junction is the critical current density J_c, which is determined by the thickness of the insulating AlO_x barrier formed in the oxidation process. From the cryogenic measurement of the dc SQUID we obtain the critical current of the Josephson junctions and then calculate out the critical current density afterwards.

We begin this section with a description of the 500 mK liquid ^{3}He cryostat and mea-

surement setup. Afterwards, we describe the I-V characteristic measurement and the magnetic field dependent critical current measurement of the dc SQUID.

3.4.1 Measurement setup

Since our Josephson junctions are made of aluminum, we need to cool down our sample to temperatures below 1.2 K which is the critical temperature for aluminum. To achieve such a low temperature, a ^{3}He evaporation cryostat is employed (cf. Fig. 3.11a). The cryostat consists of several stages. The outermost stage is a heat shielding vacuum which isolates the inner part from the environment. The next stage is a container filled with liquid ^{4}He where a Joule-Thompson process can be applied. Therefore the temperature can be further lowered to 1.5 K in order to condense ^{3}He in the innermost stage where the sample is placed. Then, we start the evaporation cooling by pumping at the liquid ^{3}He volume and approximately 500 mK can be reached in the end. More details of the cryostat are described in Ref. [14].

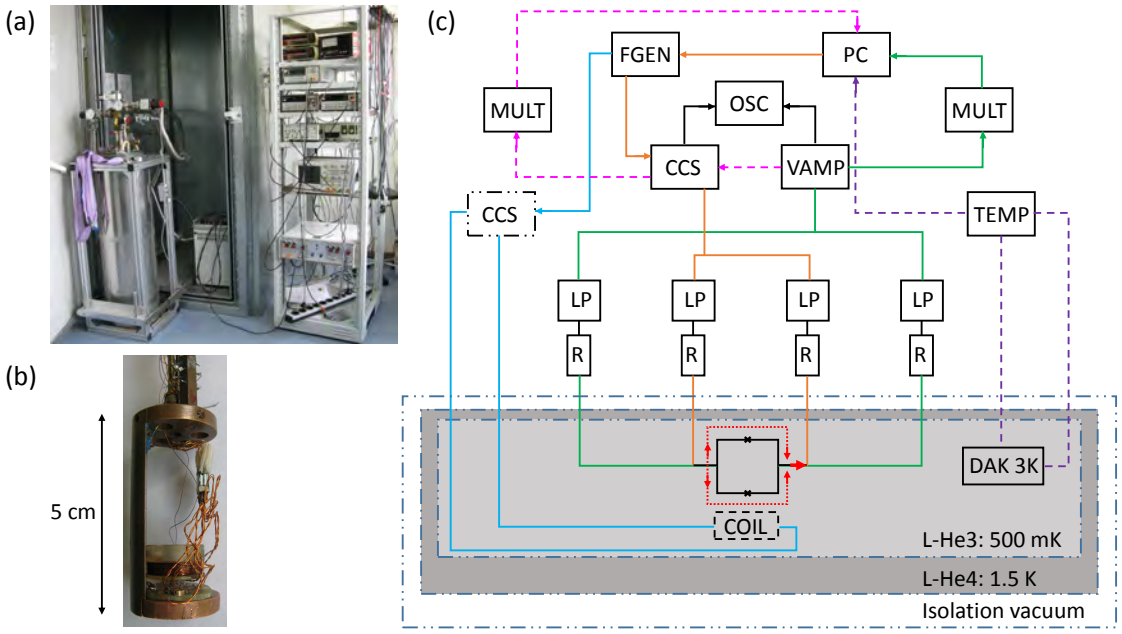

Figure 3.11: **(a)** Photograph of cryostat, measurement devices and screening chamber. **(b)** Photograph of sample holder with sample mounted inside. A superconducting coil is placed a few mm above the dc SQUID. **(c)** Schematic drawing of measurement setup: The dc SQUID is in the innermost part of the cryostat at 500 mK. The orange and green circuits are for 4-point-measurement. The dashed pink wires are for "detect" mode. Furthermore, the purple circuit connects the thermometer to the computer and the blue circuit controls the superconducting coil. All the data are collected to a LabView program in the computer. FGEN: arbitrary function generator, MULT: digital multimeter, CCS: constant current source, VAMP: voltage amplifier, OSC: oscilloscope, LP: low-pass filter, DAK 3K: calibrated resistance for temperature measurements, COIL: superconducting coil.

3.4.2 Measurement method

Usually, before cooling down, a room temperature pre-check of the sample is performed. Although no quantum phenomena can be observed at this temperature, it is helpful for checking whether all the connections, especially the aluminum bonds, work properly. Furthermore, from the measured room temperature resistance we can estimate the critical current density. Typically, a functional junction shows a room temperature resistance of approximately $100\,\Omega$ or higher. In general, small (large) room temperature resistance indicates a high (low) critical current density. For more information about this estimation see Ref. [15].

In order to protect the sample from high-frequency environmental electromagnetic fields, the whole setup is placed inside a shielding chamber during measurement. Moreover, the cryostat is also covered with a mu-metal shielding to further protect the sample inside from dc magnetic fields. Furthermore, a cryoperm magnetic shielding cover is placed around the sample holder. For measuring the magnetic field dependent critical current, a superconducting coil is fixed directly above the sample with a distance of a few mm (cf. Fig. 3.11b).

The specific behavior of a dc SQUID is already described in Sec. 2.3. By increasing the current applied to the circuit, we can observe the transition of the dc SQUID from the superconducting state to normal resistive state with a critical current I_c. To measure the *I-V* characteristic of the Josephson junctions in practice without the resistance of the leads, we perform 4-point-measurements (cf. Fig. 3.11c). The current applied to the circuit splits into the two branches of the dc SQUID (red line). A voltage drop can be observed when the junction switches to the resistive state. Actually, the applied current is a sweeping current from a constant current source driven by a function generator. Afterwards, the superconducting coil is switched on to generate an external magnetic field at the dc SQUID so that we can measure the magnetic field dependent critical current. According to Eq. (2.20), the critical current of the dc SQUID can be modulated by the external magnetic flux penetrating the SQUID loop. In the end, a LabView program is used to record the critical current as a function of the magnetic field [15].

Chapter 4

Fabrication process and results

The main goal of this thesis is to improve the fabrication stability, namely reproducibility, of the Josephson junctions. In this chapter, we present the efforts towards this goal in different steps during the fabrication process and the corresponding results. In the first section, the advantages of the new spin coater are investigated, such as the effects on the resist film thickness and the Josephson junction overlaps. Section 4.2 then deals with the tests with the new EBL system and the improvement it brings to the fabrication process. Subsequently, the cryogenic measurement results of the dc SQUIDs with different oxidation parameters in the evaporation process are discussed in Sec. 4.3. Furthermore, a new rule for the oxidation pressure and time in order to estimate the critical current density is set up there. Additionally, the last section covers several different types of hard mask.

4.1 New spin coater

As discussed in Sec. 3.1, two layers of resist should be spin coated on the substrate. The first step is to mount the substrate on the chuck of the spin coater. However, the supporting part of the fragment adapter for holding the substrate is very small (cf. Fig. 4.1a), it is difficult to mount the substrate on the same spot every time. If the mounting spot of the substrate is not fixed, the topography of the spin coated resist films will vary from run to run, which in the end will affect the fabrication reproducibility of the Josephson junction. The easiest way to solve this problem is to mount the substrate always in the center. A metal semicircle tool with a cut out specific to the chip is used for centering. The centering process is illustrated in Fig. 4.1.

4.1.1 Resist thickness

According to the Josephson junction fabrication routine at the WMI [30], we use PMMA/MA 33% as the bottom layer which can generate a thin film with a thickness of approximately 700 nm under spin speed 2000 rpm for 2 minutes. For the top layer, which will form the nm-sized bridges later, a high resolution resist, PMMA 950 k, is used.

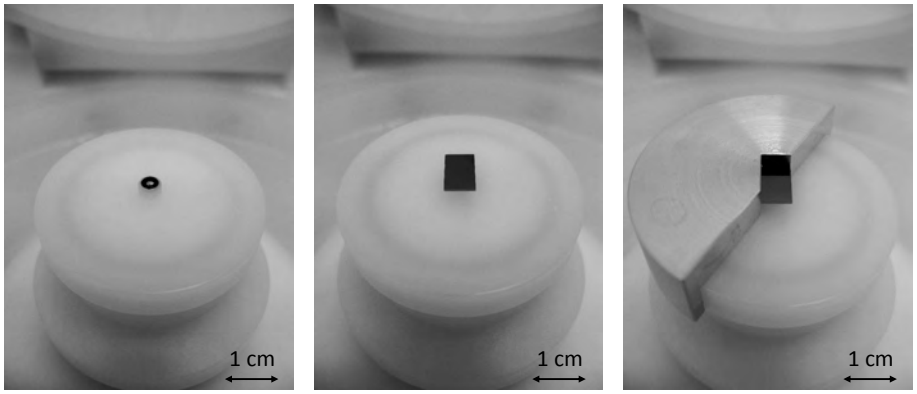

Figure 4.1: Photograph of the spin coater's sample holder. Steps for centering the substrate: First, mount the sample and turn on the vacuum pump. Second, plug on the centering tool and align the substrate. Finally, unplug the tool.

With a spin speed of 4000 rpm and a spin time of 2 minutes, a roughly 70 nm thick top resist film is produced. The photograph of a spin coated substrate is shown in Fig. 4.2. Due to the finite extent of the substrate, significantly higher film thickness at the edges of the substrate, commonly called edge beads, can be observed with bare eyes [30].

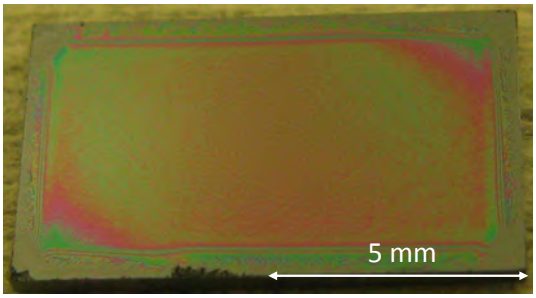

Figure 4.2: Photograph of a 6 mm×10 mm substrate with resist spin coated on.

As discussed in Sec. 3.1, the final film thickness is generally defined by the combination of spin speed and spin time. We leave these two key factors the same compared to the former process with the old spin coater, in order to analyze other effects influencing the coated resist properties. The devices used for measuring the film thickness are a dektak and an ellipsometer. The results are depicted in Fig. 4.3. The resist thickness of the bottom and top layer is approximately 685 nm and 65 nm respectively. Compared to the values obtained with the old spin coater (670 nm and 70 nm), it only differs by a few nanometers which is well within the usual error range [30]. Deviations may come from the nitrogen atmosphere and the closed bowl design. This result is expected, since spin speed and spin time are kept the same for the old and the new spin procedure. Hence, the description in Sec. 3.1 is verified by this result.

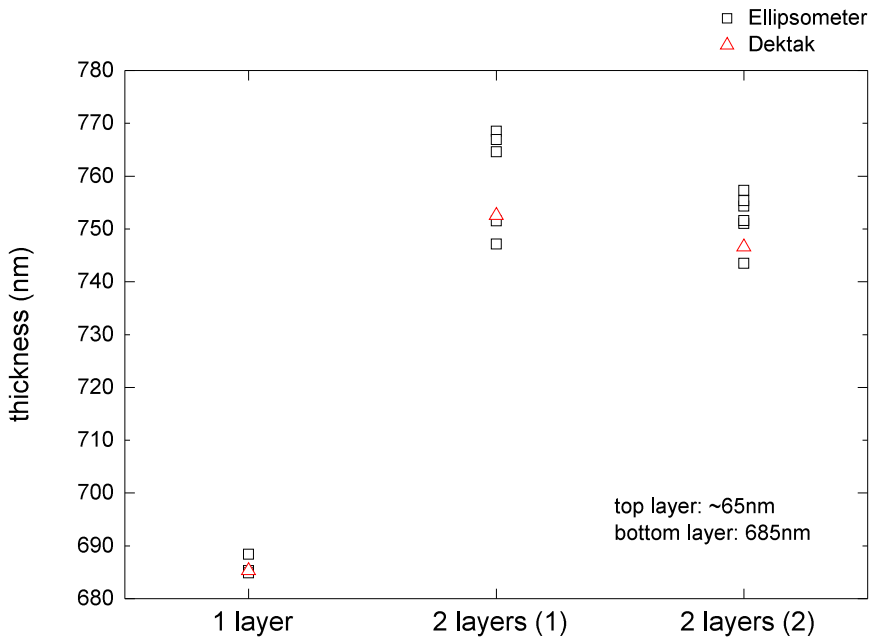

Figure 4.3: Plot of resist thickness: One sample with only bottom resist and two samples with double layer resist are measured.

4.1.2 Josephson junction overlap

The overlap area is a very crucial geometric property of a Josephson junction due to its significant influence on the quantum behavior of the dc SQUID according to the theory in Ch. 2. When it comes to scaling up the number of superconducting circuits in the future, the properties of the junctions should be identical although they are distributed over a much larger area on the wafer. Therefore, identical overlaps of Josephson junctions all over the wafer become indispensable. The overlap width is determined by the opening width of the top resist mask which is fixed for a certain pattern while the overlap length is defined by the angle of the shadow evaporation and the thickness of the bottom layer. However, deviations of the overlap might occur due to imperfections in the resist system.

For investigating the junction overlap, a SEM is employed. We measure the overlaps of the junctions from both samples fabricated with the old spin coater and the new spin coater respectively. Figure 4.4 illustrates the positions of the junctions on the substrate. The overlap length of both samples are plotted in Fig. 4.5. From the plot, it is obvious to see that the overlap length variation of sample “old” is approximately 140 nm while the overlap length of the sample “new” converges at approximately 180 nm with a variation of only 50 nm. This result indicates that the new spin coater performs approximately three times better in terms of junction overlap reproducibility. There are less than eight data points per sample because some junctions are obviously damaged. The broken junctions

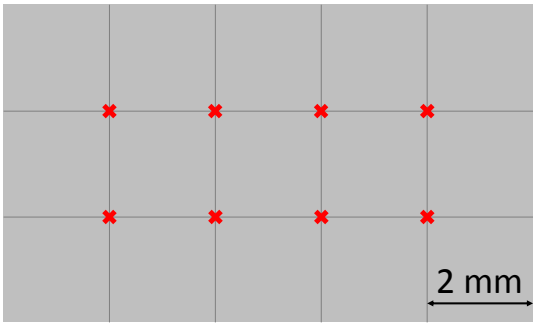

Figure 4.4: Scheme of Josephson junctions' positions on the substrate: The grey part stands for the substrate which is 6 mm×10 mm in dimension. The grids are for indicating the positions of the junctions (red crosses) on the substrate.

are attributed to a damaged resist mask, which can be caused by the effect of some dirt on the resist during EBL writing. The still existing variation of 50 nm can be traced back to the deviation of the resist bridge width, the variation of the bottom resist thickness and the image measurement error.

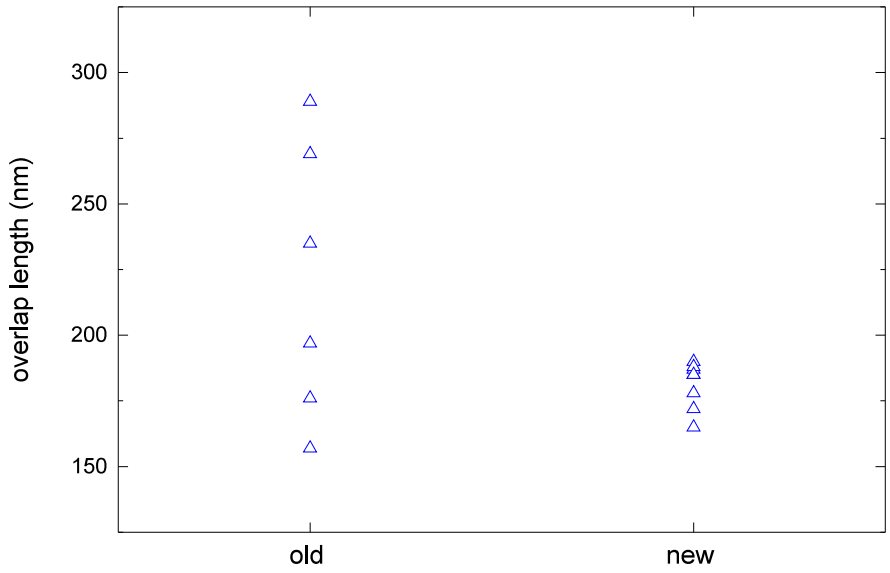

Figure 4.5: Plot of junction overlap length: Junction overlap lengths on two different samples are compared. Sample "old" is made with the old spin coater and sample "new" is made with the new spin coater.

However, the only fabrication differences between the two samples is the machine used for spin coating. Moreover, the shadow evaporation angle for junctions on the same sample is identical, so the reason for larger overlap variations can only be the bottom resist variation across the whole substrate. Figure 4.6 shows how the bottom resist thickness

variation affects the Josephson junction overlap length. If we assume the resist bridge is

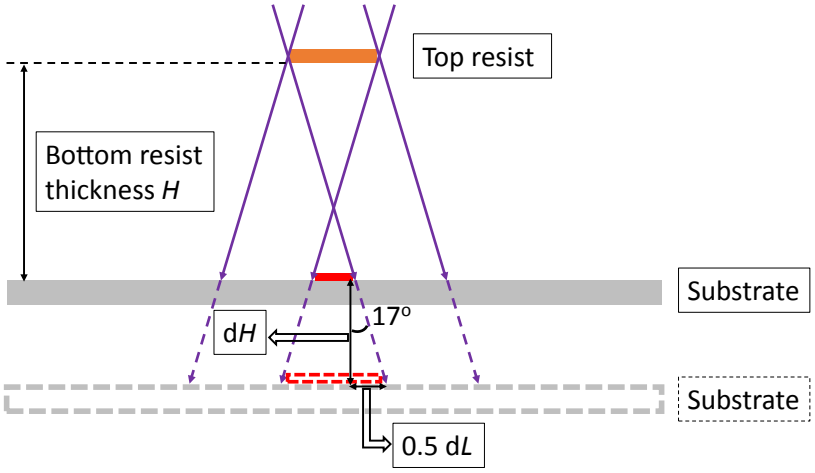

Figure 4.6: Demonstration of Josephson junction overlap length variation caused by the variation of the bottom resist thickness.

identical for all the junctions, the variation of the junction overlap length due to variations of the bottom resist thickness can by calculated via the equation

$$dL = 2\,dH\,\tan(17^\circ)\,, \tag{4.1}$$

where L is the junction overlap length and H is the bottom resist thickness. With this equation, we can calculate the bottom resist thickness variations for sample "old" and "new" are 230 nm and 80 nm, respectively. Putting the variations into relation with the total thickness of the bottom layer, it is a variation of approximately 34% and 11%.

From this point of view, our result confirms that the resist spin coated by the new spin coater is much more uniform in thickness than the one spin coated by the old machine. During the spin process, the fluid resist dries out as it moves towards the edge of the substrate. So the viscosity of the fluid resist will change with distance from the center of the substrate which can lead to radial thickness non-uniformity in the end. When the resit is dispensed onto the substrate, it starts to evaporate its solvent. Due to the "closed bowl" design, a solvent saturated atmosphere forms above the sample. This atmosphere slows down the drying process. Therefore, the viscosity remains more constant across the substrate so that the thickness uniformity of the resist film will be increased.

In conclusion, the features of the new spin coater indeed make a major contribution to the fabrication reproducibility of Josephson junctions.

4.2 New EBL system

When the substrate is spin coated, the next step is to generate the pattern on it. In this section, first we introduce the general writing process of our new EBL system. Then, we conduct performance tests for resolution, stitching and proximity effect. The results are shown and discussed. Finally, we describe the special writing process for Josephson junctions and evaluate the developed structures afterwards.

4.2.1 General writing process

In order to protect the electrons from scattering at air molecules before they hit the resist, the EBL process has to be carried out in vacuum. Our EBL system, a NanoBeam nB5 provides an airlock for transferring samples from outside into the main vacuum chamber where the writing takes place. First, we mount the spin coated sample into the slot on the chuck, then insert the chuck into the cassette which can hold up to six chucks at the same time. After that, the whole cassette is put into the airlock which will then be pumped down to $2.8 \cdot 10^{-6}$ mbar before the gate between the airlock and the writing chamber can be opened for loading the chuck into the stage inside the writing chamber by an automatic robot arm. The process of mounting the sample is demonstrated in Fig. 4.7.

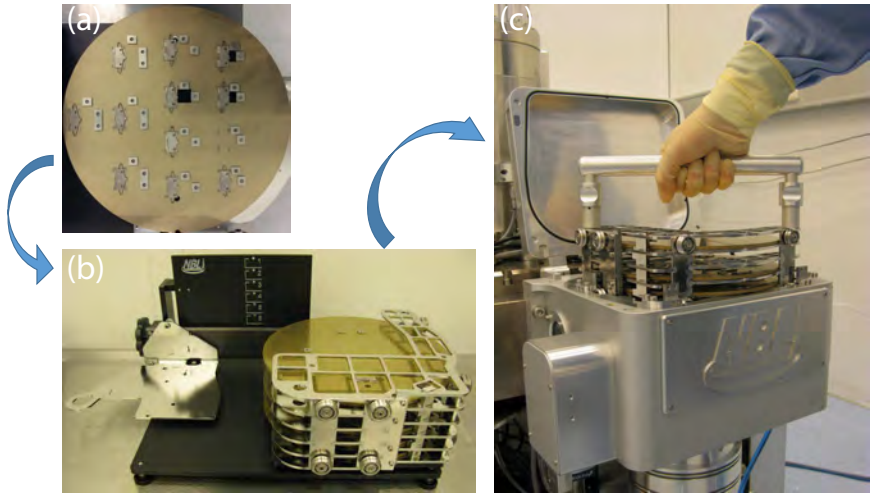

Figure 4.7: Demonstration of mounting the sample for writing: **(a)** First, the sample is mounted onto the multi-slot chuck. **(b)** Second, the chuck is inserted into a cassette which can hold 6 chucks. **(c)** Finally, the cassette is put into the airlock.

After the sample is mounted and loaded, a series of EBL parameters can be loaded from databases by software commands, including the stage height according to substrate thickness, the astigmatism, beam alignment, beam current and beam voltage. The next step is to move the stage to the correct position of the sample. Positions of the sample slots on the chuck are saved in a database and can be loaded manually to move the stage

to the corresponding position (cf. Fig. 4.8a). To focus on the sample there are two ways, one is auto-focusing with marks and the other one is manual-focusing with spherical gold particles. For the autofocus procedure, on-chip metal marks such as crosses or squares are necessary, which have to be applied close to the corners of the substrate beforehand. The size of these autofocuing structures are in the range of several micrometers. For manual focusing we need to add gold particles with a diameter of 40 nm onto the resist in advance (cf. Fig. 4.8b and Fig. 4.8c).

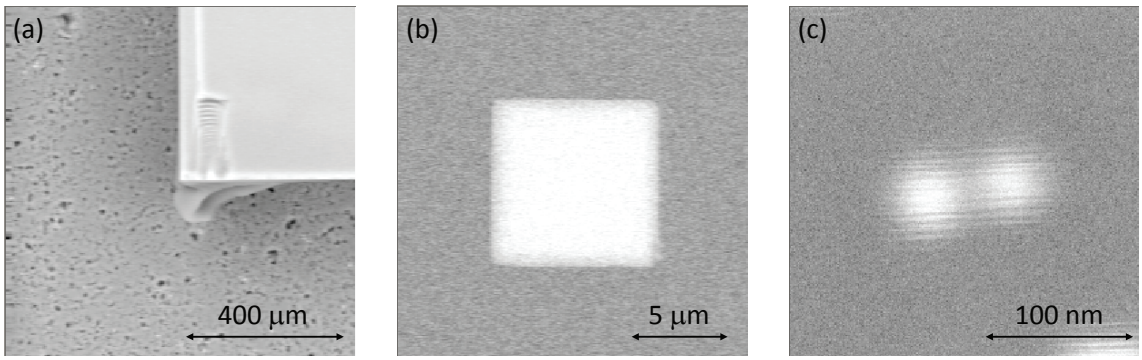

Figure 4.8: SEM images: **(a)** Find the corner of the sample. **(b)** Automatically focus on the mark. **(c)** Manually focus on the gold particles.

The patterns to be written are supplied in the well-known gds format. This gds pattern file is converted automatically into the special format which can be understood by the system. The following step is to match the pattern coordinate with the sample coordinate. This can be done by overlaying the origin of the pattern coordinate with the origin of the sample coordinate, which is usually the bottom left corner of the substrate or the center of the bottom left mark. For angle correction, we need to define another point which is usually the bottom right corner or the center of the bottom right mark. The positions of the marks on the substrate are shown in Fig. 4.9. Finally we can create the job file, which defines the writing positions of the pattern and the corresponding dose, and start writing. Due to the high beam current and special deflection technique, the writing is over 100 times faster than with our old system.

4.2.2 Performance tests

Resolution test

A flux qubit contains three Josephson junctions, two of them are equal in size and the third one has a junction area smaller by a factor of α. The width of the Josephson junctions we use is approximately 200 nm and α ranges between 0.5 and 1 [35]. Thus, the EBL system should at least be capable of writing 100 nm structures. According to the company, the resolution of this EBL system should even reach the tens of nm regime. Figure 4.10 shows

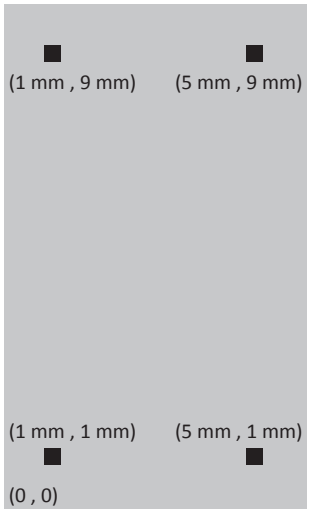

Figure 4.9: Scheme of marks' positions on the substrate: The substrate is 6 mm×10 mm in dimension. Bottom left corner is assumed to be the origin of the coordinate system. Black squares represent the marks and their positions are given in parentheses.

one of the resolution tests. The measured width of the lines is approximately 96 nm and 132 nm. Since the lines are so thin, they are a little bended during lift-off. However, the designed width for them is 50 nm and 100 nm, respectively. The deviation can be caused by the imperfect manual focusing and the image measurement error. Nevertheless, the resolution requirement for our experiments is met.

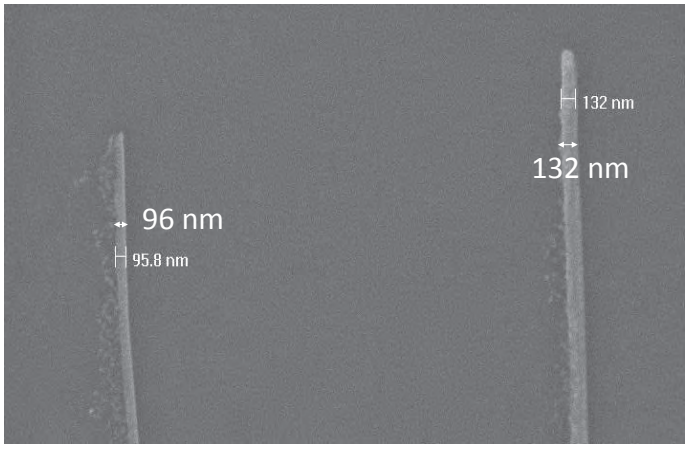

Figure 4.10: SEM micrograph of thin wires fabricated with the new EBL system.

Stitching error

Because the EBL system has a limited area of exposure (writing field), large area patterns are usually divided into many smaller writing fields, which are then stitched together by exposing side by side with stage movement between each writing field. Failure to achieve

perfect alignment between consecutive writing fields results in pattern discontinuities on the writing fields boundaries. These discontinuities are called stitching errors [36]. To minimize the stitching error, precise stage movement is required, which is achieved by monitoring the stage with a laser interferometer (cf. Sec. 3.2.2). In addition, the electron beam deflection must be adjusted to match the stage movement. This process is referred to as "writing field alignment". With the old EBL system, the writing field alignment has to be done manually while in the new system, it is done automatically and corrected dynamically during writing. Figure 4.11 compares the stitching of the test structures fabricated by our old and new EBL system, respectively. In the pattern fabricated with the old system, an approximate 700 nm stitching error is observed in the red circle. However, there is no visible stitching error in the pattern fabricated with the new system. This result indicates that the new EBL system is much better at stitching.

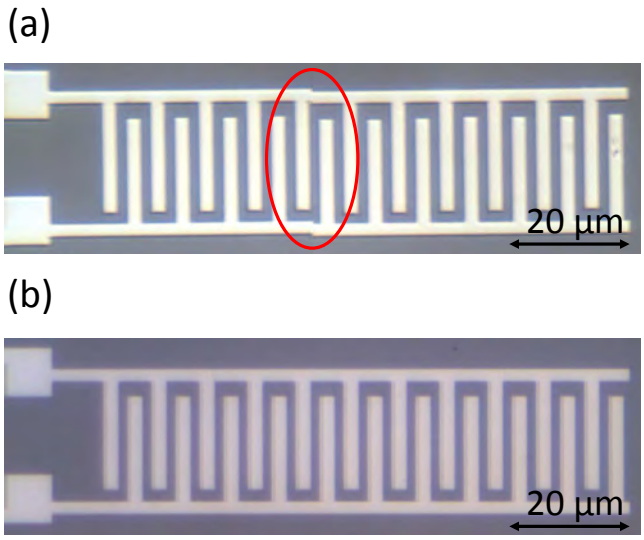

Figure 4.11: Micrograph of fabricated finger capacitors at the WMI: **(a)** Fabricated with the old EBL system. In the red circle a stitching error is observed clearly. **(b)** Fabricated with the new EBL system. There is no visible stitching error.

Proximity effect

The electron beam has a wavelength so small that the lithographic resolution is not limited by diffraction any more in our process. However, the effect of electron scattering in resist and substrate leading to undesired exposure in the regions adjacent to the incident beam limits the resolution predominantly. This effect is called the proximity effect. Any pattern can suffer significant variation from the intended size due to this effect. To reduce the proximity effect, one of the common methods is to perform dose modification by changing the dose in some parts of the pattern. For our old EBL system, the dose has to be adjusted. In contrast, for the new system, dose modification is not necessary. As described

in Sec. 3.2.2, the nB5 provides an electron beam with very sharp beam profile and almost no beam scattering. This results in no proximity effect. Figure 4.12 demonstrates the proximity effect and the dose adjustment for the old system. In Fig. 4.12(a), due to the proximity effect, the last interdigitals receive less dose than the other parts. It is impossible to meet the right dose for all parts. In Fig. 4.12(b), a dose modification is applied to the pattern. The dose for the last interdigitals is increased. For comparison, similar patterns without dose adjustment written by the new system are depicted in Fig. 4.12(c). No proximity effect is observed. All the interdigitals look almost the same.

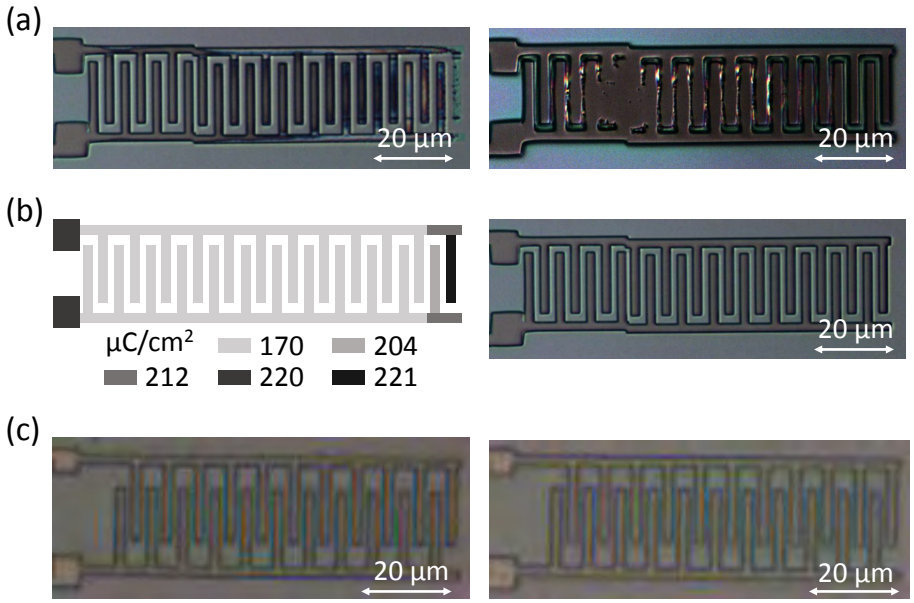

Figure 4.12: Illustration of the proximity effect in the old and the new EBL system: **(a)** Patterns without dose adjustment written by the old EBL system. It is hard to meet the right dose for all interdigitals. **(b)** Dose modification and corresponding written pattern. At the last interdigitals, the dose must be increased to compensate for the missing proximity effect. **(c)** Similar patterns without dose adjustment written by the new EBL system. All the interdigitals look identical which means no proximity effect is observed.

To conclude, in our new EBL system, the proximity effect does not play any important role any more.

4.2.3 Writing dc SQUIDs with ghost pattern

For the shadow evaporation of Josephson junctions as described in Sec. 3.3, we need undercut in a double layer resist system. The high energy electron beam can break the polymer chains in the resist making it soluble to the corresponding developer. A minimal dose (critical dose) should be reached before the polymer chains are broken. Due to an increased amount of monomers, the bottom resist is much more sensitive to the electron beam which makes it possible to generate the undercut.

In our old EBL system, the electrons of the beam are accelerated with 30 kV. The electrons scatter inside the resist then leads to an exposure of areas surrounding the pattern area which is the origin of the proximity effect. However, for generating undercut, this effect is an advantage we can make use of. The exposure dose of the scattered electrons is higher than the critical dose of the bottom resist while lower than the critical dose of the top resist. In our resist system, the dose used is around 700 µC/cm^2 for the top resist and 150 µC/cm^2 for the bottom resist. After development, the undercut necessary for shadow evaporation can form underneath the bridge area. The dc SQUID pattern we use for writing and the micrograph of the developed structure with undercut are shown in Fig. 4.13. The designed width of the junction lines is 500 nm and the junction nose is 220 nm × 308 nm. The gap at the junction area, which will serve as the bridge, is 292 nm.

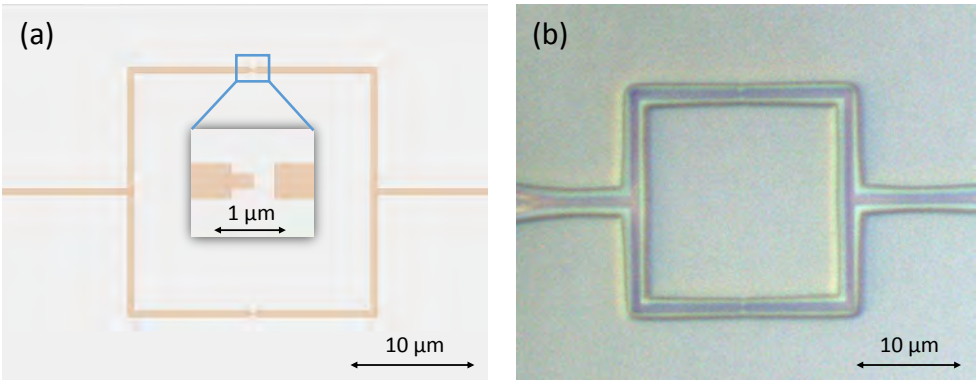

Figure 4.13: **(a)** Pattern file of the dc SQUID. The inset shows the junction nose. **(b)** Micrograph of the developed structure written with the old EBL system. The dark blue area is the pattern structure on the top resist while the light greenish area around it is the undercut.

In the new EBL system, an accelerating voltage of up to 100 kV is possible for the electrons. According to the company, this system has no beam scattering. Less beam scattering leads to straighter edges on the exposed resist. However, undercut formation

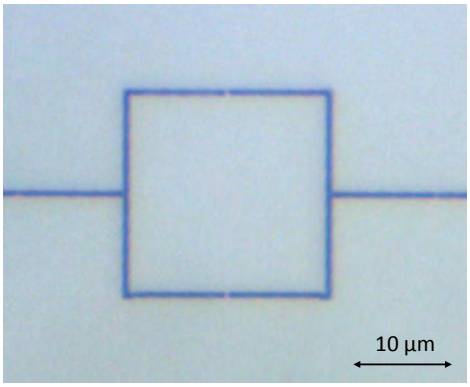

Figure 4.14: Micrograph of the pattern structure written with the new EBL system: No undercut visible, even though strongly overdeveloped.

is hard to gain with a vertical beam profile. Figure 4.14 shows the developed structure of the same pattern with over four times longer development time. Still, no undercut is observed.

As mentioned before, there is a sensitivity difference between the top and bottom resist. So we can apply a ghost pattern on the area where we want to have undercut. The ghost pattern gives the area an exposure dose higher than the critical dose of the bottom resist but lower than that of the top resist just like scattered electrons would do. The first version of the ghost pattern is depicted in Fig. 4.15.

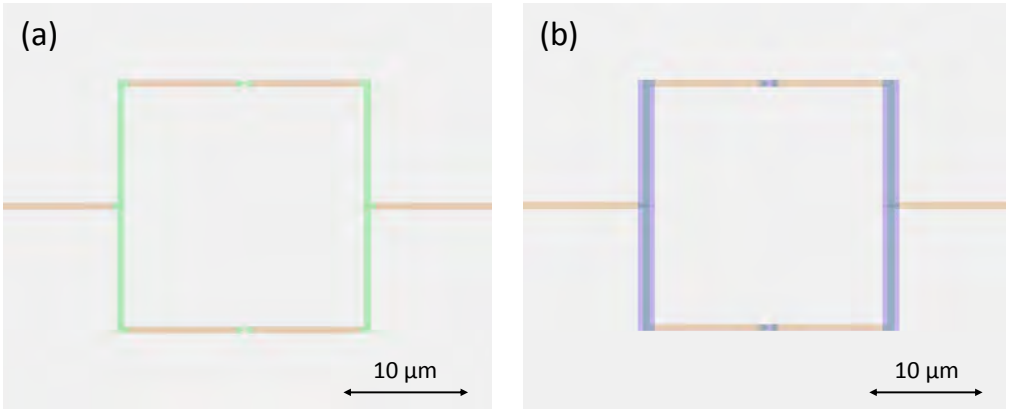

Figure 4.15: Pattern file of dc SQUID with ghost structure: **(a)** The pattern is cut into two parts. The orange parts receive the same dose as before, the green parts receive 75% of the dose. **(b)** The violet parts are added as the ghost pattern which receive the dose of 25%. In this way, the green parts receive the same dose as the orange parts.

In principle, we only need to apply the ghost pattern at the bridge area, because there the undercut is necessary. But during the evaporation process later on, the Al vapor comes in two different angles along the direction of the junction lines. If there is no

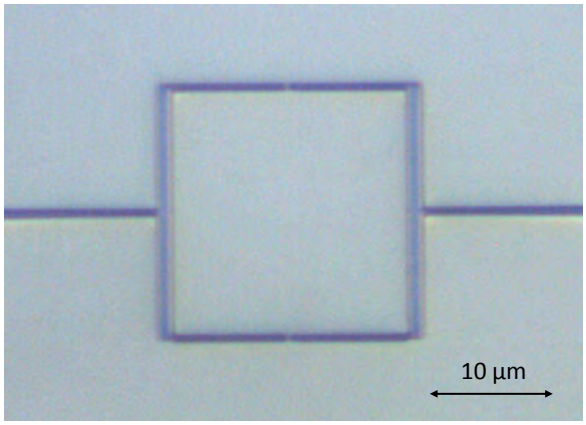

Figure 4.16: Micrograph of the developed structure of the dc SQUID with ghost pattern. The undercut is clearly observed.

undercut around the lines perpendicular to the junction lines, many of the Al atoms will

be deposited on the wall of the resist and be lifted off afterwards. Therefore, we also aim for a 400 nm undercut at each side of the vertical lines. The developed structure of the pattern is shown in Fig. 4.16.

After evaporation, the junctions are measured with the SEM. Here we find out that some junctions break into two parts and some feedlines are thinner than expected (cf. Fig. 4.17).

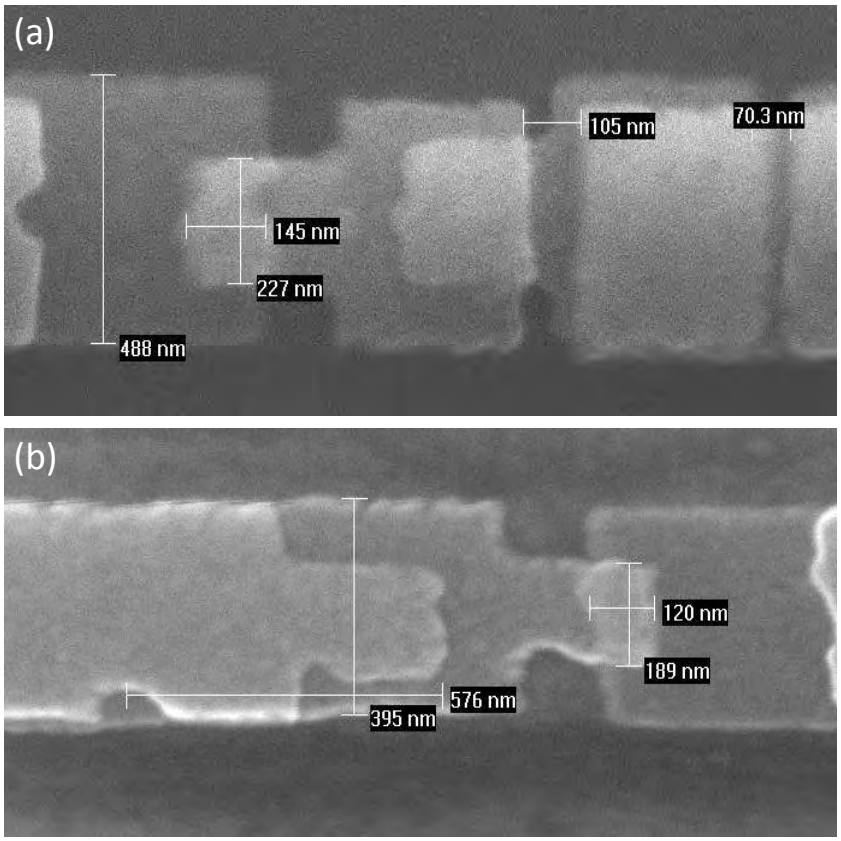

Figure 4.17: SEM micrograph of Josephson junctions before ghost pattern optimization: **(a)** Juction is separated into two parts. **(b)** Width of feedline is about 100 nm smaller than expected.

The reason for the first problem might be that the pattern is cut into two different parts and placed in different layers. Since the electron beam writes the pattern layer by layer, small variations in focusing may cause imperfect stitching of the two parts which leads to the discontinuity at the junction in the end. For the second problem, the reason could be the imperfection of the rotating stage in the evaporation chamber for two angle evaporation. If the sample is not aligned perfectly parallel to the direction of the junction lines, Al may be deposited onto the resist walls and be lifted off afterwards. As a result, the lines become thinner.

To solve these problems, we have to make some adjustments to the ghost pattern. First, the pattern is not separated at the critical positions anymore. Taking both the ghost pattern dose and the junction pattern dose into account, this method will lead to

a slight overexposure in the junction area, which is still lower than the resist's crosslink dose. Therefore, the exposed areas do not change significantly. Second, we also give the horizontal lines an undercut of 400 nm at each side just the same as the vertical lines. The new ghost pattern and the corresponding developed structure are presented in Fig. 4.18. A typical Josephson junction fabricated with optimized ghost pattern is shown in Fig. 4.19. The problems of split junctions and thinner feedlines do not exist any more.

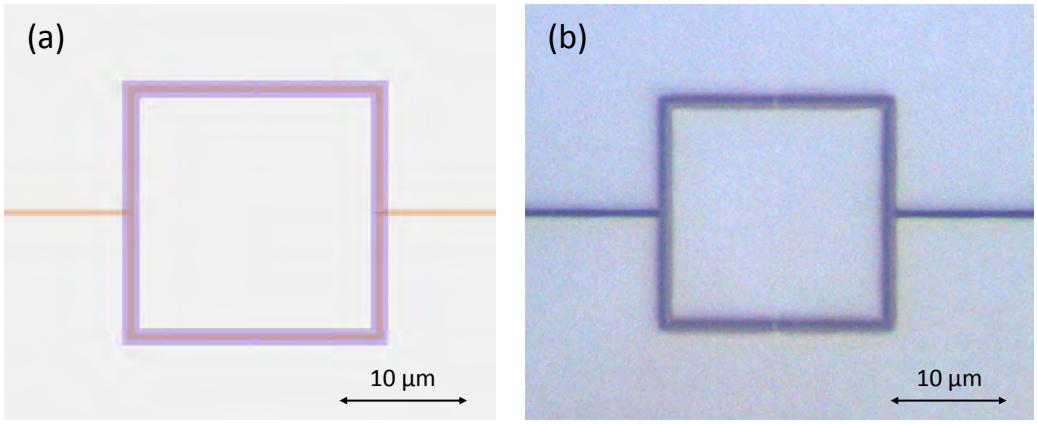

Figure 4.18: **(a)** Pattern file of the dc SQUID with a new ghost structure all over the loop area. **(b)** Micrograph of the corresponding developed structure with undercut.

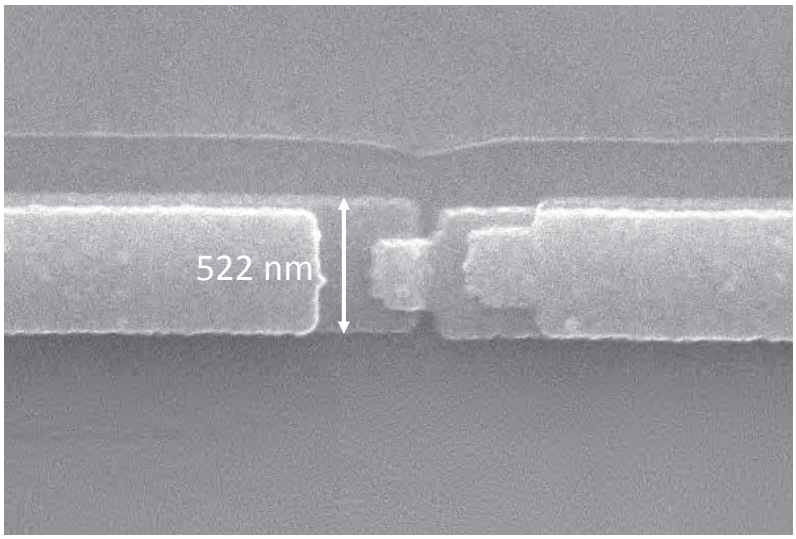

Figure 4.19: SEM micrograph of a typical Josephson junction after ghost pattern optimization.

The development methods we use are different for the patterns written by the old and new EBL system. For the patterns written by the old EBL system, the area around the pattern structure is more or less exposed by the scattered electrons. Thus, the development time needs to be controlled very carefully. For the patterns written by the new EBL system, development time is not so critical anymore. Since there is no beam scattering,

only the pattern area is exposed by the electron beam. We only need to give it a sufficient development time to make sure the exposed area is fully dissolved in the developer.

4.3 Evaporation process

So far, the substrate is spin coated with two layers of resist, patterned with EBL and developed with the corresponding developer. The next step is to deposit thin Al films. The evaporation process is already a standard process at the WMI. First, the sample is mounted on the holder which will then be transferred to the evaporation chamber (cf. Fig. 4.20). For the first evaporation, 50 nm of Al is deposited at an angle of 17°. After oxidation, a second layer of Al film with thickness of 70 nm is evaporated at an angle of -17°. Both evaporation steps employ the same evaporation rate. In this section, the parameters of the evaporation process are investigated. Additionally, the lift-off process after evaporation is discussed.

Figure 4.20: Photograph of sample holder for evaporation: There are six 6 mm × 10 mm slots on the holder. One sample is mounted onto the top middle slot.

4.3.1 Evaporation rate

The surface roughness of the first deposited Al film affects the oxidation process and thus is an important parameter for fabricating well-defined Josephson junctions. In our case, the surface roughness is determined by two factors. The first one is the substrate surface which is assumed to be constant and will not be further studied in this work. The second factor is the evaporation rate which can be tuned easily.

The rougher the Al surface is, the larger is the effective area for oxidizing. In our evaporation system, higher evaporation rates produce smoother Al films [15]. In this work, two different evaporation rates are used in order to examine their effect on the critical current density. The results are discussed in Sec. 4.4.2.

4.3.2 Oxidation pressure and time

According to Eq. (2.6), the critical current density J_c depends exponentially on the AlO_x barrier thickness d. Oxidation is a very complex process and is hard to control. In this thesis, we manipulate the oxygen pressure and oxidation time which, in combination, determine the thickness of the AlO_x barrier. Higher oxygen pressure with longer oxidation time results in a thicker oxide barrier and thus a lower critical current density.

In order to get the desired critical current density for different qubits, two sets of oxidation parameters are investigated. For superconducting flux qubits, high J_c values are needed (typically $\sim$200 A/cm^2 - 2000 A/cm^2)[11]. However, for transmon qubits, a much lower critical current density is required (typically $\sim$100 A/cm^2). The results are analyzed and discussed in Sec. 4.4.2.

4.3.3 Lift-off

When the evaporation process is done, the spare Al is removed together with the resist layer during the so-called lift-off. This process is simply done by immersing the sample into warm acetone for about 20 min and the resist together with the spare metal will peel off from the substrate. A typical evaporated structure after lift-off is shown in Fig. 4.21.

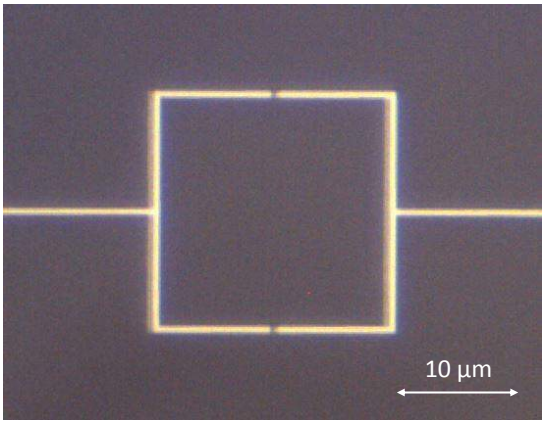

Figure 4.21: Micrograph of a typical evaporated dc SQUID after lift-off.

4.4 Cryogenic measurements

Now it comes to the characterization of the fabricated dc SQUIDs. Through the cryogenic measurements of the dc SQUIDs we can study the properties of the Josephson junctions. In this section, the wiring from the dc SQUID to the measuring devices is discussed. Afterwards, the measurement results are analyzed.

4.4.1 Wiring

Since the dc SQUIDs are very small (20 µm in dimension), they must be first connected to larger contacting pads on the substrate with feedlines. In previous fabrication routine at the WMI, 400 µm×400 µm Pt contacting pads are fabricated with optical lithography and sputtering [15]. Then, the dc SQUIDs are fabricated at corresponding positions (cf. Fig. 4.22a). However, the situation has been changed now due to the installation of the new EBL system. When writing with the old EBL system, the contacting pads have to be fabricated separately because the old EBL system is not capable of writing such big structures in an acceptable time. It might take over 20 hours to write only one sample. In contrast, the new EBL system can write much faster due to the high beam current and fast deflection. As a result, the contacting pads can be written with EBL too. It takes only 2.5 hours to write 8 of the patterns shown in Fig. 4.22(b). After development, the dc SQUIDs together with the contacting pads can be evaporated in one step.

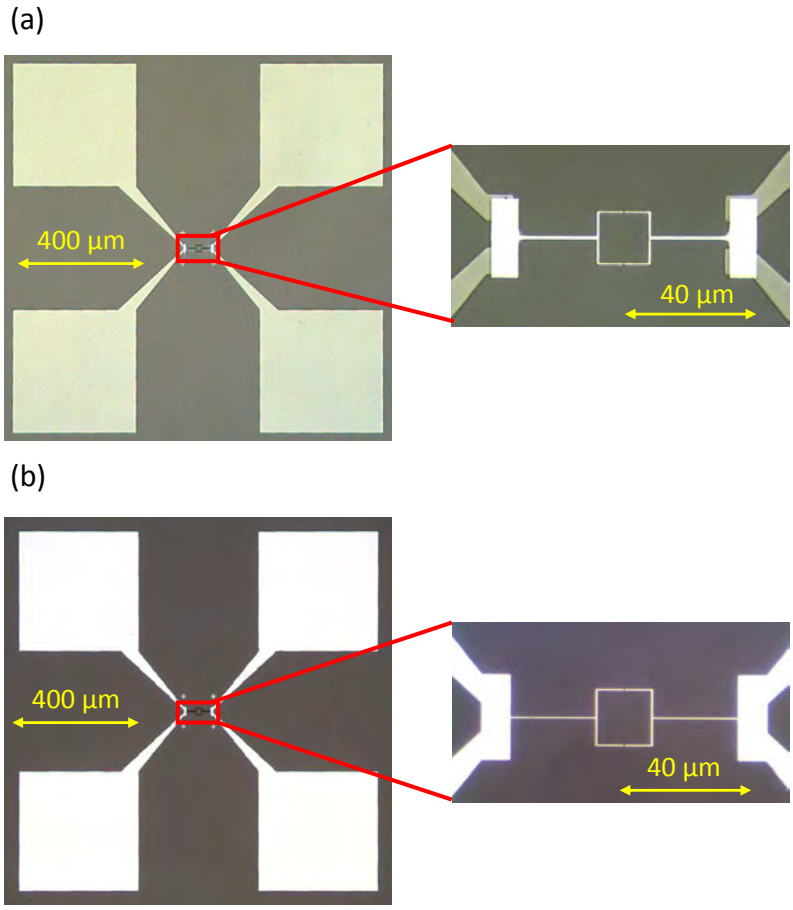

Figure 4.22: **(a)** Micrograph of the dc SQUID with contacting pads written separately. In the inset, the gray part is Pt fabricated with optical lithography and sputtering beforehand. The bright part is Al fabricated with EBL and evaporation. **(b)** Micrograph of the dc SQUID and contacting pads fully fabricated with EBL and evaporation.

Furthermore, the dc SQUIDs must be connected from the substrate to the printed circuit board which then can be connected to the measuring devices through a sample holder (cf. Sec. 3.4). This connection is realized by a reliable ultrasonic bonder (cf. Fig. 4.23a) which is a standard tool also used in electronics industry. A thin Al wire of 30 µm in diameter is applied from the copper pad of the sample holder to the contacting pad on the substrate through a needle by ultrasonic welding (cf. Fig. 4.23b). For sake of reliability, three wires are bonded for each connection. After this, the sample holder is mounted onto the sample rod for measurement.

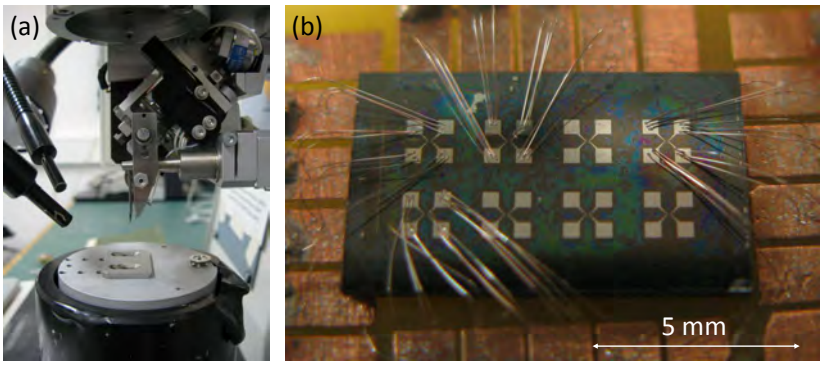

Figure 4.23: **(a)** Photograph of ultrasonic bonder with needle and thin Al wire. **(b)** Photograph of a sample connected to the printed circuit board with Al bonds.

4.4.2 Measurements

If the room temperature pre-characterization seems reasonable, the sample rod is inserted into the cryostat which will be cooled down to approximately 500 mK for measuring. In the following, the recorded I-V characteristics of our samples are shown and the results are discussed.

Current-voltage characteristics

In absence of an external magnetic field, the dc SQUID is equivalent to a single Josephson junction with critical current $2I_c$ and normal resistance $R_n/2$. The non-linear and hysteretic I-V characteristic of a typical dc SQUID with $Al/AlO_x/Al$ junctions is shown in Fig. 4.24. First, the current increases from zero while the voltage stays unchanged at zero. When the current I is increased above the switching current (here 0.365 µA), the voltage jumps and the dc SQUID switches to the normal resistive state where the voltage increases proportional to the current. Then, the current decreases until the dc SQUID returns to superconducting state again (here at 0.055 µA). In the intermediate regime between 0.055 µA and 0.365 µA the I-V curve shows a highly non-linear behavior due to the existence of quasiparticles which will not be discussed any further in this work.

With the recorded I-V curve, we can study the properties of the Josephson junctions such as the normal resistance R_n and the critical current. For this sample, R_n / 2 $\simeq 520\,\Omega$ with a systematic error in the order of approximately 10% to 20%. However, since the sample-to-sample fluctuation due to fabrication process is much larger, this error can be neglected. In ideal case, the switching current equals the critical current. However, due to noises during measurement, the measured switching current is always smaller than the critical current. According to Eq. (2.11), the $I_\mathrm{c}R_\mathrm{n}$ product for Al junctions is 286 µV. Therefore, the critical current of this SQUID can be calculated, which is $2I_\mathrm{c} \simeq 0.55\,\mu\mathrm{A}$.

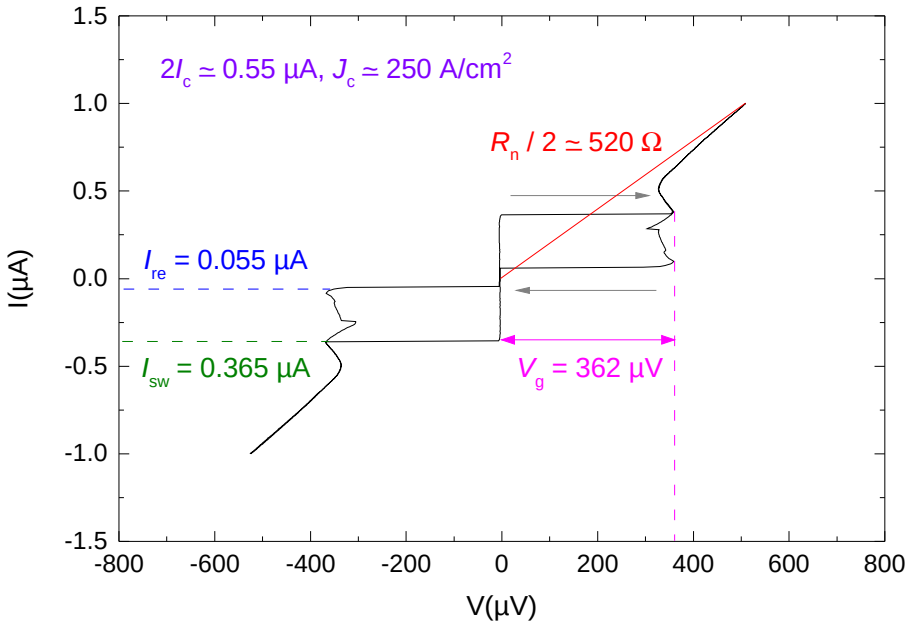

Figure 4.24: I-V characteristic of a typical dc SQUID fabricated during this work. The IVC shows a hysteretic behavior (gray arrows). The green and blue dashed lines indicate the I_sw = 0.365 µA and I_re = 0.055 µA respectively. The pink dashed line shows a voltage drop of 362 µV which is a constant for Al junctions. The normal resistance is calculated via the red line: R_n / 2 $\simeq 520\,\Omega$. Thus, the critical current $2I_\mathrm{c} \simeq 0.55\,\mu\mathrm{A}$. And with the knowledge of corresponding junction area sizes, the critical current density $J_\mathrm{c} \simeq 250\,\mathrm{Acm}^{-2}$ can also be figured out.

Switching current as a function of magnetic flux

Another characteristic property of the dc SQUID is the magnetic flux dependence of switching current. As described in Sec. 2.3, a periodic pattern of $I_\mathrm{c}(\Phi)$ is to be expected. During the measurement, a sweeping current is applied to the magnet coil, which generates a magnetic flux penetrating through the loop of the dc SQUID. The switching current

values at each coil current value are recorded by the computer. Since the loop area of the dc SQUID is fixed, the coil current corresponds to the magnetic flux. The modulated $I_c(I_{coil})$ curve of the dc SQUID characterized in Fig. 4.24 is plotted in Fig. 4.25 which does not reach zero as it is described by theory (cf. Sec. 2.3). From this plot we can read the maximum of $I_{sw} = 0.375\,\mu A$, which is the same as the value read from Fig. 4.24 within the limits of accuracy. According to Eq. (2.23), if we take the switching current as the critical current, the screening parameter for this dc SQUID can be estimated: $\beta_L \simeq 1$.

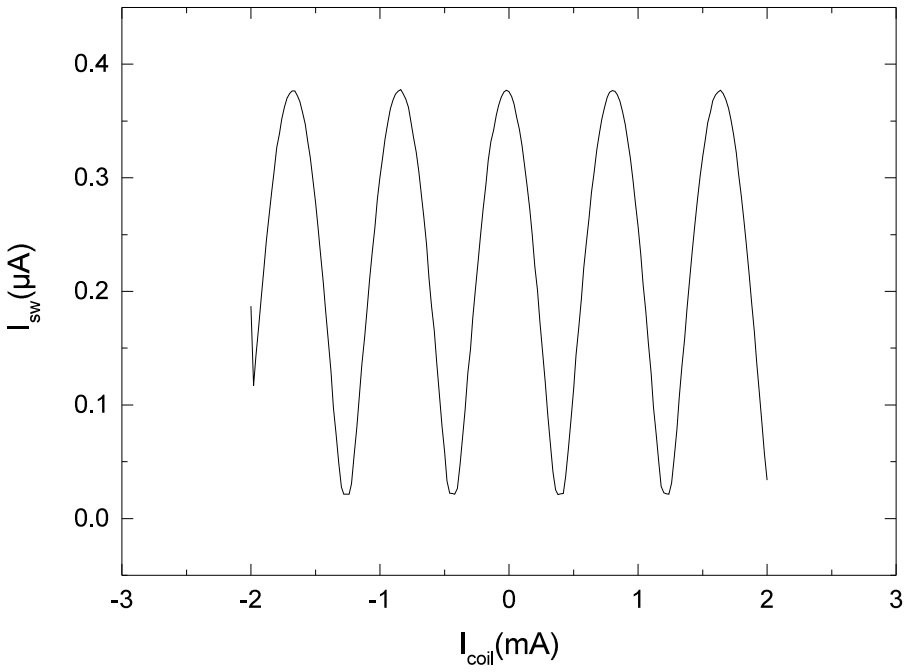

Figure 4.25: Plot of switching current in dependence of coil current which corresponds to the magnetic flux penetrating through the dc SQUID loop. The pattern is periodic as expected.

Low critical current density for transmon qubit

For further experiments, the focus of fabrication lies on the critical current density J_c. Transmon qubits need a critical current density of approximately $100\,A/cm^{-2}$ or even lower. To achieve such a low critical current density, a relatively thick AlO_x barrier is required. Therefore, high oxygen pressure and long oxidation time are needed during the oxidation process. The parameters we use for this purpose are $7.8 \cdot 10^{-3}$ mbar of pure oxygen pressure and 3000 s.

From the plotted curve in Fig. 4.26, we can see two SQUIDs have almost identical J_c of approximately $240\,A/cm^{-2}$ with a standard deviation of $20\,A/cm^{-2}$. The variation of the critical current density is very small. This result is because of the high oxygen pressure

and long oxidation time. During oxidation, after the rapid formation of the monolayer oxide, further oxidation is only possible with the tunneling of oxygen through the oxide. Therefore, after a certain time, the oxidation rate decreases exponentially with time till the oxidation stops in the end. For thicker oxide, the thickness is more stable against the fluctuations of the oxidation parameters. Hence, it is much easier to fabricate low critical current density Josephson junctions in a controlled manner.

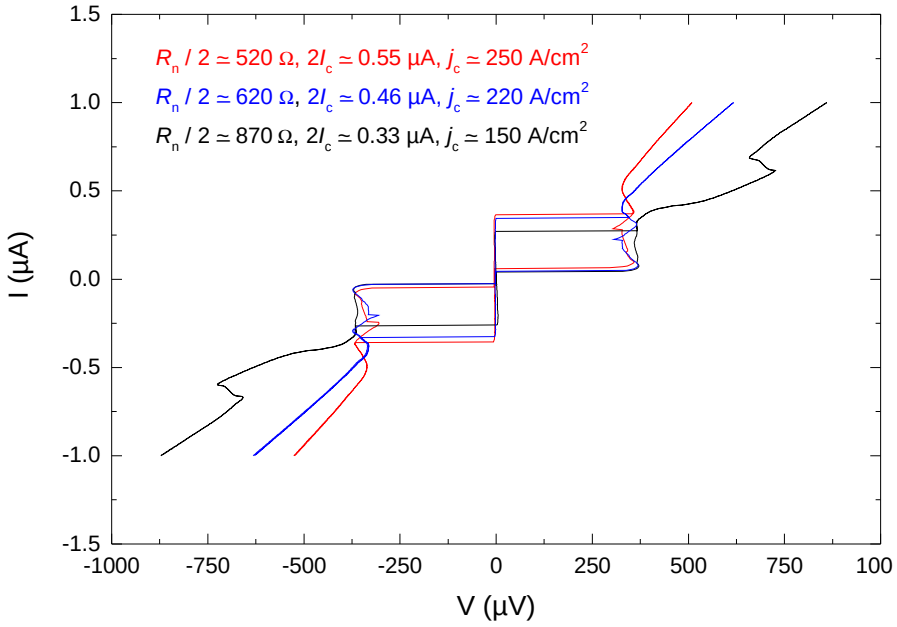

Figure 4.26: *I-V* characteristic of dc SQUIDs with low critical current density: All three dc SQUIDs are on the same substrate thus have the same fabrication parameters. Two (red and blue) of them have almost the same critical current density which is a bit higher than that of the third one (black).

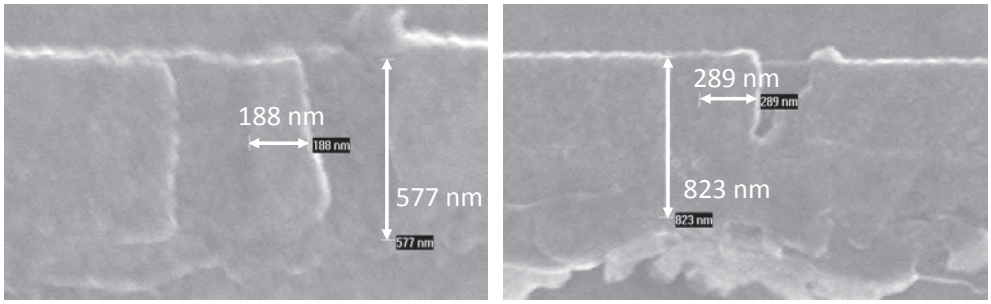

Figure 4.27: SEM images of the Josephson junctions for the third dc SQUID (black): Both of the junctions are damaged.

However, for the third dc SQUID (black), the critical current density is approximately

80 A/cm^{-2} lower than the other two. The reason is found in the Josephson junctions which are shown in Fig. 4.27. The resist masks for both junctions may have been partially damaged during the fabrication process. The reason for this damage can be some dirt on the resist affecting the EBL writing at corresponding bridge area. It is impossible to measure the the area of these two junctions precisely. Instead, we use an estimated area from the images to calculate the critical current density. Therefore the J_c value for this dc SQUID is not accurate and for reference only.

To sum up, it is now possible to use the new EBL system to fabricate Josephson junctions with stable critical current density for transmon qubit experiments.

High critical current density for flux qubit

The flux qubits require a critical current density of approximately one order of magnitude higher than the transmon qubits. We reduce the oxygen pressure and oxidize for a shorter time in order to obtain a thinner oxide barrier. However, the variation of critical current density is generally larger for junctions with a higher J_c due to the thinner oxide barrier. The aim of this work is to improve the fabrication stability of the Josephson junctions. So we try to find the intermediate critical current density for the flux qubit that can be

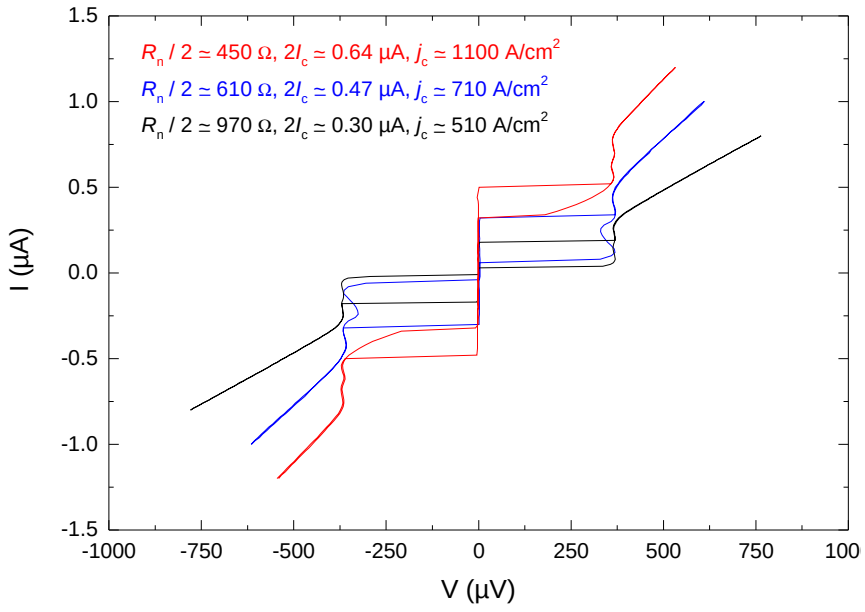

Figure 4.28: *I-V* characteristic of dc SQUIDs with high critical current desity: All three dc SQUIDs are from the same chip. The critical current density fluctuates to some degree, but is in the vicinity of 600 A/cm^{-2} .

fabricated with an acceptable fluctuation. After studying the fabrication experience at the

WMI, the target J_c value is set to $600\,\mathrm{A/cm^{-2}}$ and the oxidation parameters are adjusted to $5.2 \cdot 10^{-4}\,\mathrm{mbar}$ and 800 s.

The measurement results are plotted in Fig. 4.28. We obtain an average J_c of approximately $770\,\mathrm{A/cm^{-2}}$ with a standard deviation of $300\,\mathrm{A/cm^{-2}}$. Although we come very close to the targeted value of $600\,\mathrm{A/cm^{-2}}$, the variation is still very high. When the barrier becomes thinner, the influence of the uneven surface features (e.g. grains) on the effective barrier thickness increases. As a result, it contributes to the variation of the critical current density. Another reason for the high variation are the different positions of the dc SQUIDs on the substrate, an influence which vanishes for thicker oxide barrier. According to Ref. [37], the tunneling probability Δ of the flux qubit is proportional to $\sqrt{I_c}\exp(\sqrt{I_c})$. With this relation, we can figure out that the critical current spread of this sample can lead to a factor of 2 in the variation for Δ.

To conclude, fabrication of Josephson junctions with acceptable J_c variation for flux qubit experiments is possible now, but there is still room for improvement.

Effect of evaporation rate

As described in Sec. 4.3.1, the evaporation rate also affects the oxidation process and thus

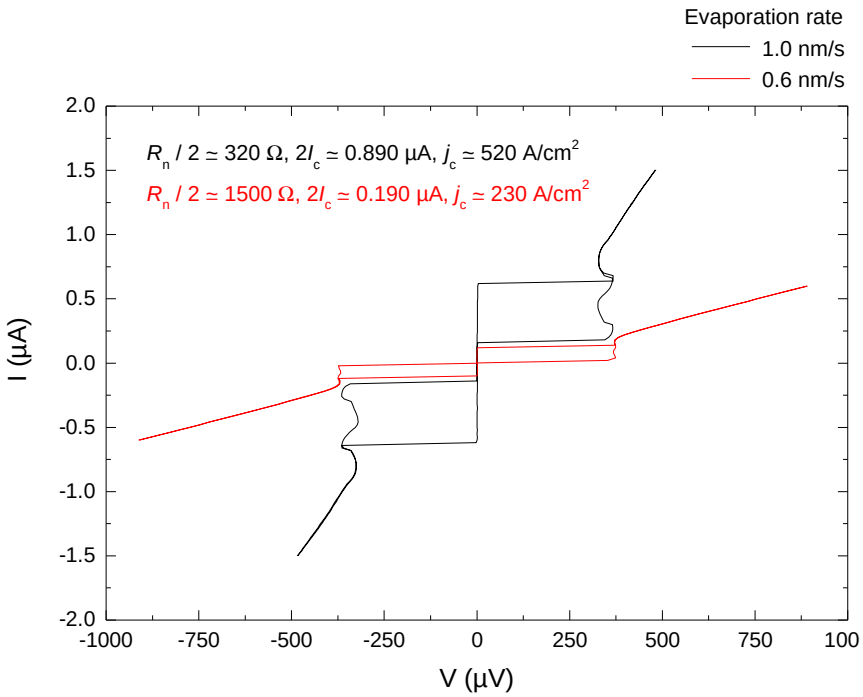

Figure 4.29: *I-V* characteristic of dc SQUIDs with different evaporation rates: Both dc SQUIDs are fabricated with the same oxidation parameters. The evaporation rate for the black one is 1.0 nm/s while for the red one is 0.6 nm/s.

plays a role in the determination of the critical current density of the Josephson junctions. For all samples discussed so far, the evaporation rate is 1.0 nm/s. In order to test the effect of the evaporation rate on J_c, we decrease the evaporation rate to 0.6 nm/s and keep the oxidation parameters unchanged which are $5.2 \cdot 10^{-4}$ mbar and 800 s. The measurement result is plotted together with another dc SQUID fabricated with evaporation rate of 1.0 nm/s in Fig. 4.29.

From the plot, the effect of the evaporation rate on the critical current density is clearly observed. The dc SQUID fabricated with evaporation rate of 1.0 nm/s (black) has a critical current density of 520 $\mathrm{A/cm^{-2}}$ which is within the variation range of the J_c achieved above for flux qubit junctions (cf. Fig. 4.28). However, the critical current density of the dc SQUID fabricated with evaporation rate of 0.6 nm/s is only 230 $\mathrm{A/cm^{-2}}$ which is much lower than 770 $\mathrm{A/cm^{-2}}$ and is beyond the variation limit. This result can be explained by the roughness of the evaporated Al films described in Sec 4.3.1. Further investigations on the topic of surface roughness goes beyond the scope of this work.

4.4.3 $P^{1/2}t$ rule

Usually, the L-product, which is the product of the oxygen pressure and oxidation time during the oxidation process, is used to estimate the critical current density of the Josephson junctions [38]. A higher L-product results in a thicker oxide barrier and thus a lower critical current density. One can map the L-product to certain critical current density values by trial and error. However, large deviations often occur when using this estimation method. Based on the theoretical equation [cf. Eq. (2.6)] of the critical current density and a theory about the oxidation of Al, a new method for estimating J_c is given in this thesis, which is the so-called $P^{1/2}t$ rule.

According to a study on the pressure dependence of the oxidation of aluminum at room temperature in 1968, which is explicable in terms of the extended Cabrera-Mott theory for the formation of very thin oxide films [39], we can obtain the equation for the thickness of the aluminum oxide barrier in dependence of oxygen pressure P and oxidation time t:

$$d^{2/3} = 6.05 \ln(138 P^{1/2} t + c) \tag{4.2}$$

where d is the oxide barrier thickness and c is a constant. In this equation, the units for d, P and t are Å, Torr and min, respectively. After converting them into nm, mbar and s, the equation can be rewritten as following:

$$d^{2/3} = 0.1913 \ln(2 P^{1/2} t + c) \tag{4.3}$$

By inserting this equation into the J_c equation [cf. Eq. (2.6)]:

$$J_c = \frac{e\hbar\kappa}{m_e} \frac{\sqrt{n_1 n_2}}{\sinh(2\kappa d)} \equiv \frac{a\kappa}{\sinh(2\kappa d)} , \tag{4.4}$$

we can get the equation of J_c in dependency of P and t:

$$J_c = \frac{a\kappa}{\sinh\left\{0.664\kappa\left[\ln(2P^{1/2}t + c)\right]^{2/3}\right\}}. \tag{4.5}$$

In this equation, we can regard J_c as a function depending only on $P^{1/2}t$, where a, κ and c are constants for a certain superconducting material. If we plot the critical current density of the Josephson junctions against $P^{1/2}t$ and fit the curve with Eq. (4.5), we can obtain the values for a, κ and c. Then this equation can be used to estimate the critical current density.

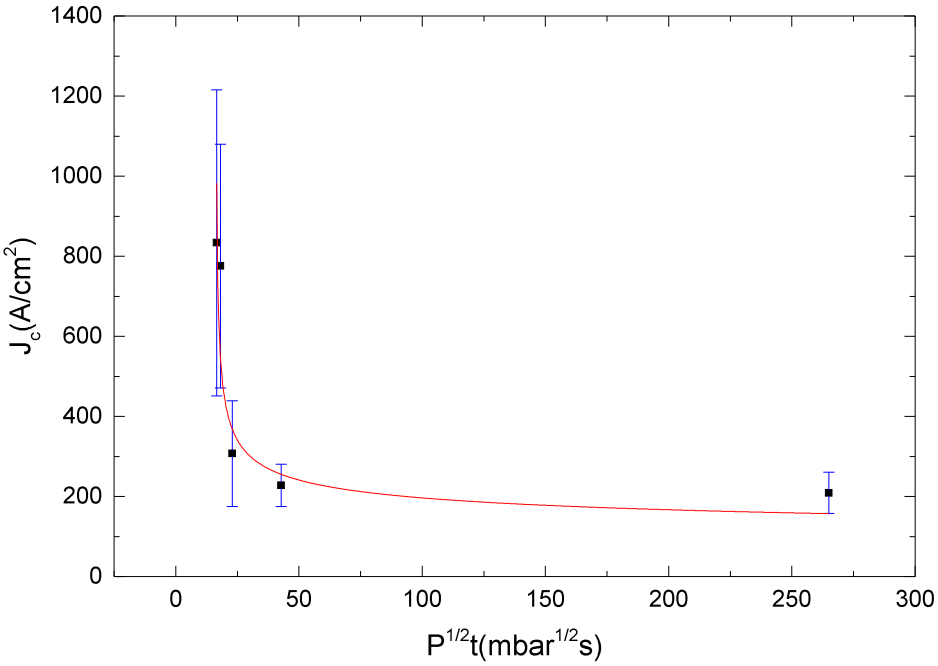

Figure 4.30: Critical current density as a function of $P^{1/2}t$: Black squares are the average J_c values for each $P^{1/2}t$ value. The error bars indicate the J_c variations at corresponding $P^{1/2}t$ values. The red line is the fitting curve by using Eq. (4.5).

Together with some other data points collected at the WMI [15], the critical current density as a function of $P^{1/2}t$ is plotted in Fig. 4.30. We can clearly see that the data points are described well by Eq. (4.5). From the graph, it is obvious that a small $P^{1/2}t$ value produces a high critical current density, whereas high $P^{1/2}t$ values result in low current densities. The error bars manifest that the critical current density has larger fluctuations at high value regime while it is more stable for lower values. The values of the fitting parameters are summarized in Tab. 4.1.

On the basis of the fitting results and the equation for the characteristic decay constant

	Fitting for J_c
$a \,/\, 10^{-7}\mathrm{Acm}^{-1}$	554.26 ± 280.70
$\kappa \,/\, \mathrm{nm}^{-1}$	0.77 ± 0.69
$c \,/\, \mathrm{mbar}^{1/2}\mathrm{s}$	-31.08 ± 1.62

Table 4.1: Fitting parameters of J_c function versus $P^{1/2}t$.

$\kappa = \sqrt{4m_e(V_0 - E_0)/\hbar^2}$, the effective barrier height can be calculated:

$$V_0 - E_0 = 11.3\,\mathrm{meV}\,.$$

This approximation is reasonable when compared to the Josephson junction coupling energy $E_J = \Phi_0 I_c/2\pi$ which is in the order of 1 meV for our junctions.

4.5 Hard mask

In circuit quantum electrodynamics, the coupling between qubits and resonators is important. The qubits used at the WMI are fabricated with Al while the resonators are fabricated with Nb and they are coupled galvanically [40], which leads to an aluminum-niobium interface. However, the Nb resonator is fabricated beforehand and its surface gets oxidized in air. Therefore, in order to get an Al-Nb transition, the NbO_x has to be removed before the Al deposition of the qubit fabrication. This procedure can be done by in situ argon ion-milling just before Al evaporation inside the evaporation chamber. But, the resist mask for shadow evaporation should not be broken during ion-milling. Thus, a hard mask is needed to protect the resist mask.

Moreover, there is another reason why we need a hard mask to protect the resist mask. Many superconducting qubits are highly sensitive to dielectric loss, and the ultra-thin resist residue on the substrate induced by lift-off process is one cause for losses [41]. Hence, a substrate cleaning is necessary before Al deposition. For this cleaning, gentle in situ argon ion-milling is applicable and thus the hard mask is indispensable for the protection of the resist mask.

In this section, different types of hard masks are tried and investigated.

4.5.1 Pt sandwich hard mask

Based on the existing apparatus at the WMI, the first material we tried for the hard mask is Pt. After spin coating of the bottom resist, 5 nm Pt is sputtered onto the resist and then the top resist is spin coated above. After this, EBL writing is carried out as usual and the exposed area of the top resist is developed. Now comes the essential step of removing Pt at the pattern area. For this procedure, a short etching with RIE is employed. In the end, the bottom resist is developed for undercut and the sample is ready for Al evaporation.

The idea and the process of making the hard mask are illustrated in Fig. 4.31.

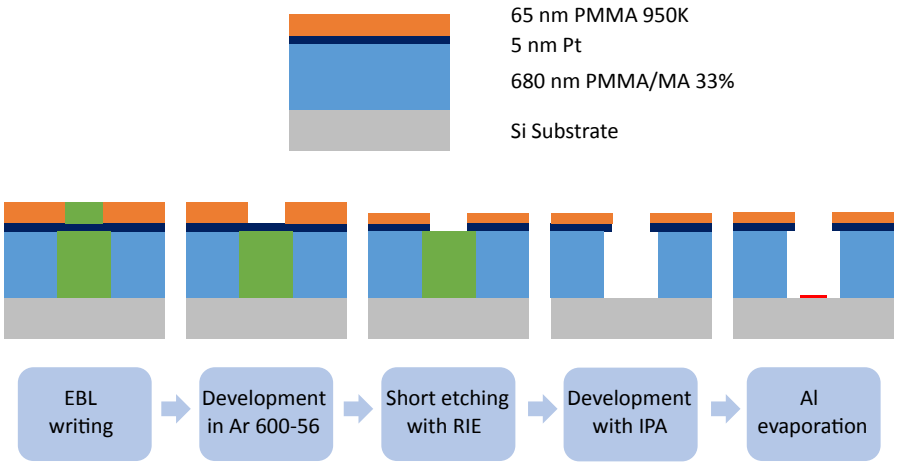

Figure 4.31: Schematic of Pt hard mask sandwich process: First, 5 nm Pt is sputtered between the two resist layers. Second, EBL writing is carried out as usual and the exposed area of the top resist is developed. Then a short etching with RIE is employed to remove Pt at the pattern area. In the end, the bottom resist is developed for undercut and the sample is ready for Al evaporation.

However, the result turns out not to be as good as expected. Figure 4.32 shows SEM images of the dc SQUID fabricated with Pt hard mask. The junction nose is completely gone. However, the 500 nm lines are still OK to some extent except in the corner. It seems like the hard mask is severely damaged. The reason might be that the etching is too strong so that the edges of the resist mask are totally etched away and even the hard mask edges are damaged. Therefore, the Pt hard mask with reactive ion etching is not a proper choice.

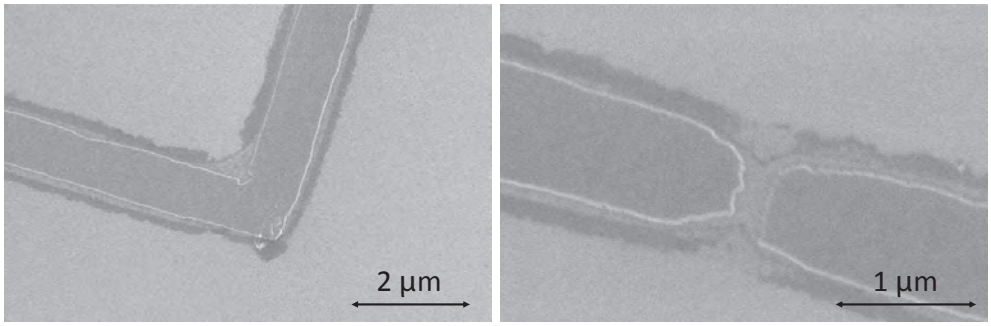

Figure 4.32: SEM micrograph of the dc SQUID fabricated with Pt hard mask: The edges of the structure are out of square and the junction nose is not visible anymore.

4.5.2 Al sandwich hard mask

Since reactive ion etching is too strong, a gentler approach is needed. At the WMI, argon ion-milling is available. Because ion-milling is much weaker, we switch from heavy Pt to light Al in order to make it possible to be milled through. The process is quite similar to the Pt sandwich mask (cf. Fig. 4.33). 5 nm Al is deposited between the two resist layers by evaporation. Then comes the EBL writing and top resist development as usual. After this, ion-milling is applied and bottom resist is developed sequentially.

Figure 4.33: Schematic of Al hard mask sandwich process: First, 5 nm Al is evaporated between the two resist layers. Second, EBL writing is carried out as usual and the exposed area of the top resist is developed. Then ion-milling is employed to remove Al at the pattern area. In the end, the bottom resist is developed for undercut and the sample is ready for shadow evaporation.

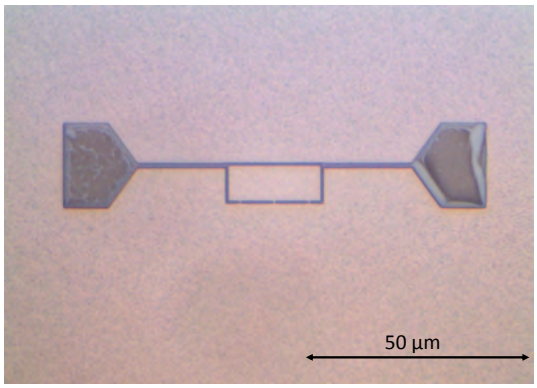

Figure 4.34: Micrograph of the test structure with Al hard mask. The argon ions are accelerated with 30 kV and the milling time is 64 minutes. There is still a lot of Al left at the edges and many Al fragments drop down to the substrate.

The result is depicted in Fig. 4.34. However, it looks not quite satisfactory. There is still a lot of Al left at the edges even the milling time is already over an hour. Moreover,

the Al does not vanish significantly much more upon further increasing the milling time. On the other hand, at the milled-through area, some Al fragment drops down to the substrate and becomes very hard to remove. The unwanted residues will then affect the Al deposition during shadow evaporation. Thus, Al hard mask with ion-milling is not suitable either.

4.5.3 Hard resist

The reason why the resist mask needs to be protected is that it is too weak for argon ion-milling and thus can be damaged very easily. To realize the protection, our previous idea is to fabricate a proper metallic hard mask. However, if the top resist can be replaced by another high-resolved EBL resist which is strong enough for ion-milling, the hard mask is not necessary any more. Such a desired resist (hard resist) is commercially available. It is the AR-P 6200.04 resist from Allresist GmbH. In this part, ion-milling test and fabrication of Josephson junctions with the hard resist are investigated.

Ion-milling test

Replacing the normal top layer resist, a 70 nm thin film of hard resist is spin coated on the bottom layer resist. In order to test the effect of the ion-milling on the hard resist, we

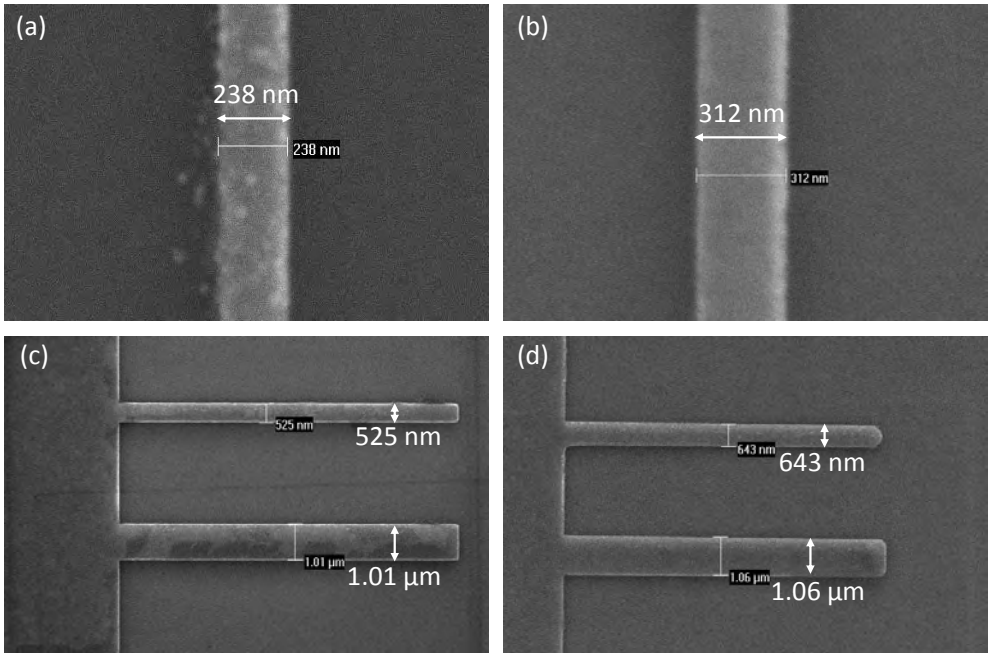

Figure 4.35: SEM images of ion-milling test: The designed width of the lines are 200 nm, 500 nm and 1 µm. **(a)** and **(c)** are lines fabricated without ion-milling. **(b)** and **(d)** are lines fabricated with 30 min ion-milling before evaporation.

pattern a set of lines and compare the width difference between the lines with and without

ion-milling treatment. The ions are accelerated with 30 kV before they hit the target. To make sure an obvious influence can be observed, the milling time is set to 30 min.

From the SEM images, we can obviously see the substrate is much cleaner after ion-milling (cf. Fig. 4.35). The grain-like "dirt" and black blocks in image (a) and (c) do not exist any more in image (b) and (d), which are treated with ion gun cleaning. On the other hand, one can also notice that the lines fabricated with ion-milling treatment are wider than those fabricated without ion-milling and get rounded at the corners. The width difference is approximately 80 nm for all the lines. However, this width difference is the result of a milling time of 30 min which is one order of magnitude longer than usual ion gun cleaning time. Therefore, we estimate the width difference can be controlled to be only a few nm after an usual ion gun cleaning with a milling time of a few minutes.

Fabrication of Josephson junctions with hard resist

Before the hard resist can be used for the fabrication of Josephson junctions, a couple of

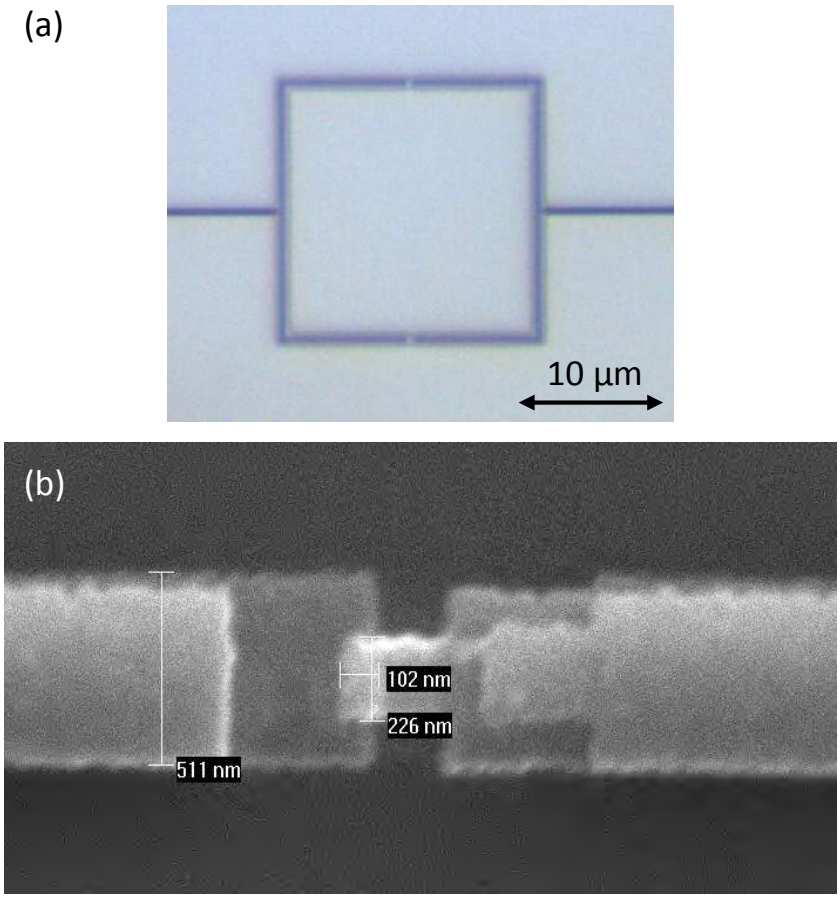

Figure 4.36: **(a)** Micrograph of developed pattern fabricated with hard resist. Undercut is clearly observed. **(b)** SEM micrograph of a Josephson junction fabricated with hard resist.

tests have to be performed. The key point of the tests is to generate a proper undercut.

Firstly, the double layer resist system is spin coated on the substrate with hard resist as the top layer. Then, we pattern a 20×40 grid of test structures with a base dose ranging from 20 µC/cm^2 to 820 µC/cm^2. The relative dose for ghost pattern is ranging from 0.05 to 0.95. After EBL writing, the developer AR 600-529 is used for development. At low dose region, no pattern is observed. This is because the dose here is below the critical dose for both resists. From the visible structures, however, no undercut is observed. The reason can be that the critical dose for the bottom resist is higher than that of the hard resist for this developer. When the ghost pattern dose is increased from 0.05 to 0.95, either no undercut is generated or the hard resist above the undercut is developed as well. For the following tests, we pattern the same structures but use MIBK as developer. After several rounds of dose and development tests, a proper undercut is generated in the end (cf. Fig. 4.36a). When MIBK is used as developer, the base dose and relative ghost pattern dose are figured out to be 800 µC/cm^2 and 0.3, respectively. Finally, Josephson junctions are fabricated successfully with hard resist (cf. Fig. 4.36b). However, the edges of the structure is a bit wavy. This can be traced back to the development of the resist mask. Since MIBK develops the hard resist much slower, small parts of the resist may remain at the edges. We argue that, the smoothness of the structure edges can be improved by longer development time.

Summing up, the hard mask issue has been solved by replacing the normal top resist with the hard resist.

Chapter 5

Summary and Outlook

The main goal of this work is to optimize the fabrication process and improve the fabrication reproducibility of Josephson junctions. Since the properties of qubits are very sensitive to the fabrication parameters, the fabrication process must be controlled as precise as possible.

First, we investigate the newly installed spin coater at the WMI. In order to minimize the non-reproducibility caused by the variation of the substrate's mounting position, we design a tool which assures the substrates are always mounted on the center of the holder. From the convergence of the junction overlaps, we find the resist spin coated by the new spin coater is much more uniform in thickness, which makes a great contribution to the fabrication reproducibility.

For EBL writing, we conduct some performance tests. The result turns out that our new EBL system is capable of writing fine structures down to the tens of nm regime. The ability of writing with almost no stitching error or proximity effect makes the fabrication more precise and reproducible. However, a new issue about the undercut appears, which used to be generated by the proximity effect. To solve this problem, we apply a ghost pattern for the undercut area, which gives rise to an additional benefit of well controlling the undercut.

Regarding the evaporation and oxidation, we fabricate dc SQUIDs with different evaporation rates and oxidation parameters. These samples are characterized by cryogenic measurements. From the nearly identical critical current densities around $240\,\mathrm{A/cm^{-2}}$, we conclude that it is possible to fabricate Josephson junctions with stable critical current density for transmon qubit experiments at the WMI. For flux qubits, we figure out a proper J_c value of approximately $770\,\mathrm{A/cm^{-2}}$. The J_c variation of the fabricated Josephson junctions can lead to a factor of 2 in the variation for the tunneling probability Δ of the flux qubit. This result demonstrates that the fabrication of Josephson junctions for flux qubits at the WMI has reached a reasonable degree of reproducibility. With help of the Al oxidation theory, we set up a new rule of oxidation pressure and time ($P^{1/2}t$) for estimating the critical current density.

In the attempt of protecting the resist mask during ion gun cleaning, we try two different metal hard masks and finally overcome this issue by replacing the top resist of

the double-layer resist system with a hard resist. After ion gun cleaning, the substrate surface is much cleaner and the hard resist degradation can be controlled to a few nm.

For future fabrication processes, we want to confirm the $P^{1/2}t$ rule for estimating critical current densities produced by different oxidation parameters. The fitting of J_c versus $P^{1/2}t$ can be improved by obtaining more data points from characterizing more dc SQUIDs. Concerning the hard resist, one can perform more tests and figure out the safe intensity of ion-milling it can bear. These tests should be performed before employing the ion-milling for removing the resist residue, which might be one of the reasons inducing the large fluctuations of critical current density. In addition, we plan to fabricate Josephson junctions which are deposited onto an ion gun cleaned surface, to see the coherence times of qubits increase.

Appendix A

Fabrication parameters

A.1 Double layer resist

	Double layer EBL resist
Bottom resist	PMMA-MA 33 %
Amount of resist	60 µL
Acceleration time	1 s
Rotation speed	2000 rpm
Spin duration	120 s
Baking	160 °C for 10 min
Top resist	PMMA 950K A2
Amount of resist	30 µL
Acceleration	1 s
Rotation speed	4000 rpm
Spin duration	120 s
Baking	160 °C for 10 min
EBL	nB5 from NanoBeam Limited
Base dose	750 µC/cm^2
Relative dose for ghost pattern	0.22
1st development	MIBK
Development temperature	room temperature
Development time	60 s
2nd development	IPA
Development temperature	room temperature
Development time	120 s
Stopping	blow-dry with nitrogen

Table A.1: Spin coating and EBL writing parameters of double layer resist.

A.2 Hard resist

	Hard resist as top layer
Hard resist	AR-P 6200.04
Amount of resist	30 µL
Acceleration	1 s
Rotation speed	4500 rpm
Spin duration	60 s
Baking	150 °C for 1 min
EBL	nB5 from NanoBeam Limited
Base dose	800 µC/cm^2
Relative dose for ghost pattern	0.3
1st development	MIBK
Development temperature	room temperature
Development time	60 s
2nd development	IPA
Development temperature	room temperature
Development time	30 s
Stopping	blow-dry with nitrogen

Table A.2: Spin coating and EBL writing parameters of hard resist.

A.3 Evaporation and oxidation

	Shadow evaporation
Pre-pressure	$< 10^{-8}$ mbar
Angle	$\pm$ 17°
Evaporation rate	10 Å s^{-1}
Thickness bottom layer	50 nm
Thickness top layer	70 nm
Oxidation time	800 s / 3000 s
Oxidation pressure	$5.2 \cdot 10^{-4}$ mbar / $7.8 \cdot 10^{-3}$ mbar

Table A.3: Evaporation and oxidation process parameters.

A.4 Ion-milling

	Ion-milling
Ion gun	tectra IonEtch Sputter Gun
Ar flow	0.5 sccm
Arm rotation in-axis	45°
Arm tilt	−20° off target and 70° on target
MW power ion gun	20 mA
Extraction voltage	-600 V
Acceleration voltage	2.4 kV
Exposure time	30 min

Table A.4: Ion-milling parameters.

Bibliography

[1] R. P. Feynman, "Simulating Physics with Computers", International Journal of Theoretical Physics **21**, 467 (1982).

[2] D. Deutsch, "Quantum computation", Physics World (1992).

[3] S. Weisner, Tech. Rep., Association for Computing Machinery, Special Interest Group in Algorithms and Computation Theory (1983).

[4] A. Zeilinger, *Dance of the Photons: From Einstein to Quantum Teleportation* (Farrar, Straus & Giroux, New York, 2010).

[5] B. Schumacher, "Quantum coding", Physical Review A **51**, 2738 (1995).

[6] J. Q. You and F. Nori, "Superconducting Circuits and Quantum Information", Physics Today **58**, 42 (2005).

[7] M. H. Devoret and R. J. Schoelkopf, "Superconducting Circuits for Quantum Information: An Outlook", Science **339**, 1169 (2013).

[8] T. Orlando, S. Lloyd, L. Levitov, K. Berggren, M. Feldman, M. Bocko, J. Mooij, C. Harmans, and C. van der Wa, "Flux-based superconducting qubits for quantum computation", Physica C **372-376**, 194 (2002).

[9] J. E. Mooij, T. P. Orlando, L. Levitov, L. Tian, C. H. van der Wal, and S. Lloyd, "Josephson Persistent-Current Qubit", Science **285**, 1036 (1999).

[10] B. D. Josephson, "Possible new effects in superconductive tunnelling", Physics Letters **1**, 251 (1962).

[11] Y.-L. Wu, H. Deng, H.-F. Yu, G.-M. Xue, Y. Tian, J. Li, Y.-F. Chen, S.-P. Zhao, and D.-N. Zheng, "Fabrication of Al/AlOx/Al Josephson junctions and superconducting quantum circuits by shadow evaporation and a dynamic oxidation process", Chin. Phys. B **22**, 060309 (2013).

[12] H. Knoglinger, "Herstellung und Charakterisierung von supraleitenden Phasen Qubits", Diploma thesis, Technische Universität München (2004).

[13] M. Göoppl, "Quantenelektronik mit supraleitenden Bauelementen - Herstellung und Charakterisierung von Fluss-Qubits", Diploma thesis, Technische Universität München (2006).

[14] K. F. Wulschner, "Nb/AlOx/Nb Josephson-Kontakte für supraleitende Quantenschaltkreise", Diploma thesis, Technische Universität München (2011).

[15] E. Xie, "Optimized fabrication process for nanoscale Josephson junctions used in superconducting quantum circuits", Master's thesis, Technische Universität München (2013).

[16] A. G. Fowler, M. Mariantoni, J. M. Martinis, and A. N. Cleland, "Surface codes: Towards practical large-scale quantum computation", Physics Review A **86** (2012).

[17] H. K. Onnes, "The resistance of pure mercury at helium temperatures", Communication from the Physical Laboratory at the University of Leiden **120b, 122b and 124c** (1911).

[18] W. Meissner and R. Ochsenfeld, "Ein neuer Effekt bei Eintritt der Supraleitfähigkeit", Naturwissenschaften **21**, 787 (1933).

[19] O. Madelung, *Introduction to solid-state theory: revised and partly rewritten translation of Festkörpertheorie* (Springer, Berlin and and Heidelberg [u.a.], 1996).

[20] L. Cooper, "Bound Electron Pairs in a Degenerate Fermi Gas", Physical Review **104**, 1189 (1956).

[21] J. Bardeen, L. N. Cooper, and J. R. Schrieffer, "Theory of Superconductivity", Phys. Rev. **108**, 1175 (1957).

[22] R. Gross and A. Marx, *Applied Superconductivity: Josephson Effect and Superconducting Electronics* (2005), lecture notes.

[23] B. Josephson, "Possible new effects in superconductive tunnelling", Physics Letters **1**, 251 (1962).

[24] M. Hermele, G. Refael, M. P. A. Fisher, and P. M. Goldbart, "Fate of the Josephson effect in thin-film superconductors", Nature Physics **1**, 117 (2005).

[25] I. Giaever, "Energy Gap in Superconductors Measured by Electron Tunneling", Physical Review Letters **5**, 147 (1960).

[26] W. C. Stewart, "Current-Voltage Characteristics of Josephson Junctions", Applied Physics Letters **12**, 277 (1968).

[27] V. Ambegaokar and A. Baratoff, "Tunneling Between Superconductors", Physical Review Letters **10**, 486 (1963).

[28] D. McCumber, "Effect of ac Impedance on dc Voltage–Current Characteristics of Superconductor Weak–Link Junctions", Journal of Applied Physics **39**, 3113 (1968).

[29] J. Clarke and A. I. Braginski, eds., *The SQUID Handbook: Fundamentals and Technology of SQUIDs and SQUID Systems* (Wiley-VCH Verlag GmbH & Co. KGaA, 2004).

[30] F. Sterr, "Optimization of Josephson Junction Nanofabrication for Superconducting Quantum Circuits", Diploma thesis, Technische Universität München (2013).

[31] *Spin Coating Theory*, Brewer Science Inc. (2008).

[32] *Specification and Accptance of nB5 Electron Beam Lithography System*, NanoBeam Limited (2014).

[33] *Introduction Excellence in Electron Beam Lithography*, NanoBeam Limited (2014).

[34] G.J.Dolan, "Offset masks for lift-off photoprocessing", Applied Physics Letters **31** (1977).

[35] J. Goetz, "Gradiometric flux quantum bits with tunable tunnel coupling", Diploma thesis, Technische Universität München (2011).

[36] R. K. Dey and B. Cui, "Stitching error reduction in electron beam lithography with in-situ feedback using self-developing resist", Journal of Vacuum Science & Technology B **31** (2013).

[37] M. J. Schwarz, "Gradiometric tunable-gap flux qubits in a circuit QED architecture", Ph.D. thesis, Technische Universität München (2014).

[38] A. W. Kleinsasser, R. E. Miller, and W. H. Mallison, "Dependence of Critical Current Density on Oxygen Exposure in Nb-AlOx-Nb Tunnel Junctions", Applied Superconductivity **5**, 26 (1995).

[39] J. E. Boggio, "The Pressure Dependence of the Oxidation of Aluminum at 298K", Surface Science (1969).

[40] P. Summer, "Characterization of superconducting coplanar waveguide resonators at millikelvin temperatures", Master's thesis, Technische Universität München (2014).

[41] C. M. Quintana, A. Megrant, Z. Chen, A. Dunsworth, B. Chiaro, R. Barends, B. Campbell, Y. Chen, I.-C. Hoi, E. Jeffrey, J. Kelly, J. Y. Mutus, P. J. J. O'Malley, C. Neill, P. Roushan, D. Sank, A. Vainsencher, J. Wenner, T. C. White, A. N. Cleland,

and J. M. Martinis, “Characterization and reduction of microfabrication-induced decoherence in superconducting quantum circuits”, Applied Physics Letters **105** (2014).

Acknowledgment

First of all, I want to thank God, my Heavenly Father, for creating me so that I can learn about the world He created. I am always grateful to Him for saving me and giving me hope to live in this world.

Then, I would like to express my thankfulness to all people who helped and supported me during this thesis:

Prof. Dr. Rudolf Gross for giving me the opportunity to perform the research phase of my master at the Walther Meißner Institut. He is always helpful to his students.

Edwar Xie for his supervision and kindness all the time. I am particularly grateful to him for teaching me all the stuff carefully and patiently. From him, I have learned the basic scientific literacy. In addition, I want to thank him for the corrections of this thesis. Working with him was so wonderful and fruitful.

Dr. Frank Deppe for welcoming me to the qubit group and correcting this thesis. He is always nice and helpful to his colleagues and students.

Matthias Pernpeintner, *Max Häberlein* and *Friedrich Wulschner* for their keen help during my experiments.

All my office mates for their company and the warm atmosphere in our office.

Besides, I also want to say thank you to:

Markus Drehsel for his tremendous help in the early days of life in Germany.

Cynthia Leung for coming into my life and accepting me as who I am.

My family for their unlimited support no matter where I am.